

POLITECNICO DI TORINO

*Master Degree in Biomedical Engineering*



**Single Bare Metal Stent  
for Aortic Arch Aneurysm Repair**

**Supervisor:**

Prof. Umberto Morbiducci

**Co-Supervisors:**

Ing. Diego Gallo

Ing. Giuseppe De Nisco

**Candidate:**

Giovanni Forini



*a mia Madre*

*-Fammi una sorpresa, lasciami stupire  
Ecco la mia resa, un sorriso comparire  
Sono un gran perdente, sono un vincitore  
Non mi importa niente mi si spalanca il cuore-  
(Può)*

# Abstract

Aneurysm consists in a focal dilation of a blood vessel compared to its physiologic diameter, due to the loss of collagen and elastin in the wall. If untreated, aneurysm could expand and, eventually, rupture causing severe hemorrhages or, in worst cases, death. Its formation and development are still not completely clear. Several studies have revealed that local inflammatory responses, leading to infiltration, in vessel layers, of particles, such as macrophages, neutrophils, lymphocytes and Mast cells, represent the necessary conditions for aneurysmal diseases insurgence. Among the different factors inducing wall inflammatory responses, hemodynamics play a relevant role. Unfavorable shear stresses exerted by flowing blood at the vascular wall, in particular, might damage the endothelial layer, carrying to atherogenic plaque (low and oscillatory wall shear stress (WSS) values) or aneurysm (high WSS values) development.

Aneurysms mainly develop at aortic or brain arteries wall. Treatment typically results in a minimally invasive procedure consisting in the implantation of a tubular metallic mesh called “stent”, in order to reestablish the physiological blood flow. Stent principal purpose is to shield the aneurysm wall from stresses, isolating it from the blood flow and decreasing blood velocity in the aneurysmal sac, preventing its rupture. However, the efficacy of an implanted stent, in restoring physiological conditions, depends on local hemodynamic patterns, geometry and body response at the disease site. For this reason, during the last decades, the interest of companies in computational fluid-dynamics (CFD) as supporting, predicting and investigating tool, during vascular devices design, has raised.

In this contest, the aim of this work is to investigate the efficacy of a single layer metal stent in computational models of thoracic aorta, affected by fusiform-shape aneurysm. Three vessels with different curvatures were investigated: two models were idealized, and one was patient-specific. The analysis was conducted by computing both WSS- and helicity-based descriptors (i.e., TAWSS, OSI, RRT, LNH,  $h$  indices).

Results showed that the efficacy of the investigated stent depends on the curvature of vascular district. It resulted to work better for straight vessels with

respect to curved ones. In all the investigated districts, stent implantation leads to (1) a decrease of blood velocities in the aneurysm sac, preventing aneurysm rupture, and (2) an increase of dynamic pressure at the outlet sections of computational models with respect to the inlet ones.

However, the investigated vascular device revealed to be incapable to efficaciously isolate the aneurysm sac, independently of vascular curvature. For this reason, a possible future development could consist in the optimization of stent weft in order to improve its efficacy in restoring physiological conditions in vascular districts affected by fusiform-shape aneurism formation.

# Contents

<b>1</b>	<b>Introduction</b>	<b>1</b>
1.1	Cardiovascular System.....	2
1.1.1	Blood Vessels.....	2
1.1.2	Arteries.....	3
1.1.2.1	The Aorta.....	4
1.1.3	Blood.....	6
1.2	Aortic Aneurysm.....	8
1.2.1	Aneurysms of the Aortic Arch.....	11
1.2.2	Rupture Risk Predictors.....	13
1.3	Aneurysm Treatments.....	14
1.3.1	Endovascular Aortic Repair (EVAR).....	14
1.3.2	Flow-Diverting Stents (FDSs).....	16
1.3.3	Multiple Overlapping Uncovered Stents (MOUS).....	18
1.3.4	Treatments' Failure: Endoleak.....	19
1.3.5	Treatment's Failure: Migration.....	20
1.4	Aim of the Study.....	21
<b>2</b>	<b>Materials and Methods</b>	<b>22</b>
2.1	Aortic Models with Aneurysm.....	23
2.2	Stent Models.....	24
2.3	Computational Mesh.....	26
2.3.1	Mesh Sensitivity: Steady-State Simulations.....	27
2.3.2	Mesh Sensitivity Analysis.....	28

2.4	Unsteady-State Simulations.....	30
2.4.1	Governing Equations.....	30
2.4.2	Computational Settings and Boundary Conditions.....	31
2.5	Post-Processing Analysis.....	32
2.5.1	Wall Shear Stress (WSS).....	33
2.5.2	WSS-Based Predictors.....	34
2.5.2.1	Time Averaged Wall Shear Stress (TAWSS).....	34
2.5.2.2	Oscillatory Shear Index (OSI)...	35
2.5.2.3	Relative Residence Time (RRT)	35
2.5.3	Helicity.....	36
2.5.4	Helicity-Based Descriptors.....	36
2.5.4.1	Local Normalized Helicity (LNH)...	37
2.5.4.2	Quantitative Helicity Indexes.....	38
<b>3</b>	<b>Results</b>	<b>40</b>
3.1	Velocity Distribution.....	41
3.2	WSS-Based Descriptors.....	43
3.3	Helicity-Based Descriptors.....	57
3.4	Pressure Distribution.....	60
<b>4</b>	<b>Discussion and Conclusions</b>	<b>68</b>
	<b>Bibliography</b>	<b>71</b>

# List of Figures

1.1	Circulatory System Scheme.....	3
1.2	Anatomy of the Human Aorta.....	5
1.3	Representation of blood vessels.....	7
1.4	Representation of main blood particles.....	8
1.5	A) Aneurysm formation scheme.....	10
	B) Mechanism of aneurysm rupture and thrombus formation.....	11
1.6	Classification of aneurysms of the transverse aortic arch.....	12
1.7	EVAR implantation technique.....	15
1.8	Aneurysm's flow velocity reduction with FDS.....	17
1.9	MOUS conformation and cell properties.....	19
2.1	Aortic Models.....	24
2.2	Stent Models and final models made of aortic.....	25
2.3	A) Meshes bodies for Unstented models.....	26
	B) Meshes bodies for Stented models.....	27
2.4	Example of mesh sensitivity for model 3NS.....	29
2.5	Inlet flowrate waveform.....	32
2.6	Velocity distribution and WSS in a lumen vessel.....	34
2.7	Helicity representation.....	37
3.1	Mean Velocity distribution.....	41
3.2	Peak Velocity distribution.....	42
3.3	TAWSS distribution, frontal view.....	44
3.4	TAWSS distribution in the intrados and extrados zones for models 2NS 2S 3NS 3S.....	45
3.5	TAWSS 20 <sup>th</sup> percentile representation, frontal view.....	46
3.6	TAWSS 20 <sup>th</sup> and 10 <sup>th</sup> percentile extrados ad intrados zones for models 2NS 2S 3NS 3S.....	47
3.7	OSI distribution, frontal view.....	48
3.8	OSI distribution in the intrados and extrados zones for models 2NS 2S 3NS 3S.....	49

3.9	OSI 80 <sup>th</sup> percentile distribution for all models in their frontal view and in the intrados and extrados zones of models 2NS 2S 3NS 3S...	50
3.10	OSI 90 <sup>th</sup> percentile distribution for all models in their frontal view and in the intrados and extrados zones of models 2NS 2S 3NS 3S...	51
3.11	RRT distribution for all models, frontal view.....	52
3.12	RRT distribution in the intrados and extrados zones for models 2NS 2S 3NS 3S.....	53
3.13	RRT 80 <sup>th</sup> percentile distribution for all models in their frontal view and in the intrados and extrados zones of models 2NS 2S 3NS 3S...	54
3.14	RRT 90 <sup>th</sup> percentile distribution for all models in their frontal view and in the intrados and extrados zones of models 2NS 2S 3NS 3S...	55
3.15	LNH Mean distribution.....	57
3.16	LNH Peak distribution.....	58
3.17	Static pressure gradient for models 1NS 1S.....	60
3.18	Static pressure gradient for models 2NS 2S.....	61
3.19	Static pressure gradient for models 1NS 1S.....	61
3.20	Dynamic pressure gradient for models 1NS 1S.....	62
3.21	Dynamic pressure gradient for models 2NS 2S.....	62
3.22	Dynamic pressure gradient for models 3NS 3S.....	63
3.23	Static Pressure at inlet and outlet surface for model 1NS 1S.....	63
3.24	Static Pressure at inlet and outlet surface for model 2NS 2S.....	64
3.25	Static Pressure at inlet and outlet surface for model 3NS 3S.....	65
3.26	Dynamic Pressure at inlet and outlet surface for model 1NS 1S.....	65
3.27	Dynamic Pressure at inlet and outlet surface for model 2NS 2S.....	66
3.28	Dynamic Pressure at inlet and outlet surface for model 3NS 3S.....	67

# List of Tables

1. Example of mesh sensitivity for model 3NS. ....	29
2. Percentile values of WSS-Based descriptors.....	43
3. Percentage values of WSS-Based descriptors percentiles.....	56
4. Quantitative Helicity Indexes for all models.....	59

# Chapter 1

## Introduction

This section focuses on the medical background of my thesis. It starts with a general introduction of the cardiovascular system and the definition of aortic aneurysms, focusing on aneurysms of the aortic arch. Subsequently the histology, pathology and the methods used to prevent rupture are discussed. In conclusion, the current treatment options and the research goal has been explained.

# 1.1 Cardiovascular System

Cardiovascular system is an organ system that permits blood to circulate and transport oxygen and nutrients to and from the cells in the body. It is composed by the heart, the blood vessels and the blood flowing into them. Cardiovascular System is subdivided in two main circulatory loops: the *Pulmonary Circulation* and the *Systemic Circulation*. The right side of the heart supports the pulmonary circulation that transports deoxygenated blood to the lungs, where the blood picks up oxygen and returns it to the left side of the heart. From this side, starts the systemic circulation which carries highly oxygenated blood to the rest of the body. The heart is a hollow muscular organ that pumps blood throughout the entire system. The human heart has four chambers: two receiving chambers called *Atria* and two discharging chambers called *Ventricles*. Referring to a complete heartbeat, a cardiac cycle is composed of *Systolic Phase* and *Diastolic Phase*. During Systolic Phase the heart pumps blood into the *Ventricles (Atrial Systole)* and then out of the heart itself (*Ventricular Systole*). During Diastolic Phase (both *Atrial* and *Ventricular*) the heart is relaxed and the blood can fill the chambers.

## 1.1.1 Blood Vessels

Blood vessels are the part of the system that allow blood to efficiently flow from the heart throughout the body and back again. There are three types of vessels: *The Arteries*, which carry the high-pressure blood away from the heart, *The Capillaries*, which allow exchange of substances between blood and tissues, and finally *The Veins*, which carry the blood from the capillaries back to the heart. Moving away from the heart, vessels progressively branch and their diameter decreases. They, usually, have three distinct layers: the external layer is called *Tunica Adventitia (or Externa)*, the middle layer is called *Tunica Media*, and the innermost layer, that faces directly the blood, is the *Tunica Intima*. (Figure 1.3)

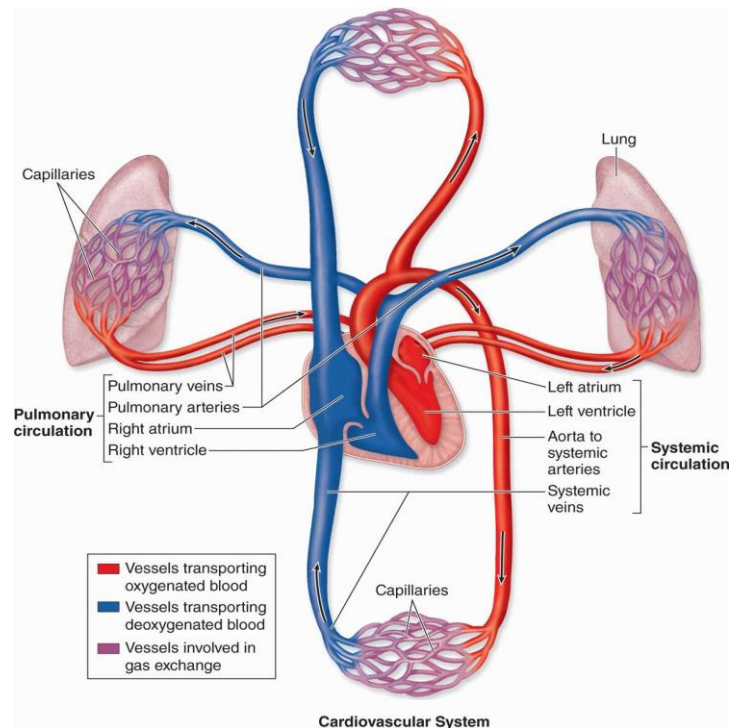


**Figure 1.1:** Cardiovascular System Scheme

## 1.1.2 Arteries

According to their dimensions, arteries are classified in: *Large Diameter Arteries* (or *Elastic Arteries*), *Medium Diameter Arteries* (or *Muscular Arteries*) and *Arterioles*, with a diameter smaller than 2 mm. In the arteries, the innermost layer, the tunica intima, is formed from a single layer of endothelial cells (EC). EC layer is the single barrier between blood and thrombogenic tissues, for this reason its compaction is fundamental to maintain the vessel's healthy structure. The intima is separated from the media by an *Internal Elastic Lamina* (IEL), the most external component of the intima. This lamina, composed of elastin, is fenestrated to allow the diffusion of substances to nourish cells deep in the vessel wall. Furthermore, through these fissures, muscle cells of tunica media can penetrate the tunica intima. The tunica media is composed of Vascular Smooth Muscle Cells (VSMC) and Elastic Tissues (ET). VSMC are responsible for vessels dilatation and constriction; the oxygen and nutrients, that are necessary to do VSMC's function, are carried through diffusion from tunica

adventitia. They also synthesize collagen, PGAG and elastin, which establish the mechanical behavior of the vascular wall. In arteries, the media layer has a thinner fenestrated *External Elastic Lamina* (EEL), which separates it from the tunica adventitia. The tunica Adventitia is made of connective tissue, fibroblasts, ET, nerves and some small vessels called *Vasa Vasorum*. Those vessels, during atherosclerosis process, can penetrate to the tunica media through the fenestrated lamina causing a structural weakening of the vascular wall. Large diameter arteries include the *Aorta*, the *Subclavian*, the origin of *Pulmonary arteries* and the beginning of the *Common Carotid artery*; the structure of their tunica media has a predominant composition of ET, for this reason they are also known as *Elastic Arteries*. Besides, medium and small arteries have an intima composition made of a thicker muscular tissue, and they are also known as *Muscular Arteries*. Muscular cells are responsible for the propagation of the systolic impulse and they are settled in different helicoidal layers that help the blood flow through the vessel.

## ***The Aorta***

The aorta is the largest artery of the human body. Originating from the left ventricle of the heart, with the *Aortic Valve*, and extending down on the abdomen, the aorta allows the distribution of oxygenated blood to all the organs of the body through the systemic circulation. The aorta is commonly divided into four sections: The *Ascending Aorta*, the *Aortic Arch*, the *Descending Aorta* or *Thoracic Aorta*, and the *Abdominal Aorta*. The aorta sections are generally similar but vary in function and histology. Ascending aorta travels superiorly and eventually becomes continuous with the aortic arch, which begins at the level of the upper border of the second stercostal articulation where it subsequently makes a hairpin turn and passes downward at the level of the fourth thoracic vertebra, becoming continuous with the descending aorta. Located just distal to aortic valve there's another portion of the aorta called the *Aortic Root*. This portion contains three small pockets, called the *Aortic Sinuses* (or *Sinuses of Valsalva*), situated between the cusps of the tricuspid aortic valve and the wall of the ascending aorta. The left sinus contains the origin of the *Left Coronary Artery*, while the right sinus contains the origin of the *Right Coronary Artery*; these two

vessels provide blood to the wall of the heart. The aortic arch gives rise to three major branches: starting proximally and extending distally is the *Brachycephalic Trunk*, which nourishes the right head and neck regions along with the right arm and chest wall, the *Left Common Carotid* and the *Left Subclavian* arteries, which supply the left portions of the collar bone. The aortic arch contains baroreceptors and chemoreceptors that relay information concerning blood pressure, blood pH and carbon dioxide levels. The thoracic aorta gives rise to several important arteries, namely the *Intercostal* and *Subcostal* arteries along with variable branches to the esophagus, pericardium and mediastinum. The abdominal aorta gives rise to the two *Renal Arteries* and many other branches of the *Visceral Arteries*; it terminates at a bifurcation draining into the *Left* and the *Right Iliac Arteries*. (Figure 1.2) As mentioned before, the aorta is classified as an elastic artery because of the considerable component of elastic lamella in the tunica media. This lamella is fenestrated and is an organized distribution of elastic fibers, type II collagen, proteoglycans and glycosaminoglycans and it's developed through the longitudinal direction. The elastic matrix present within the tunica media has a dominant role in the mechanical properties of the aorta, allowing it to distend in order to accommodate the large blood volume it receives from the heart during systole.

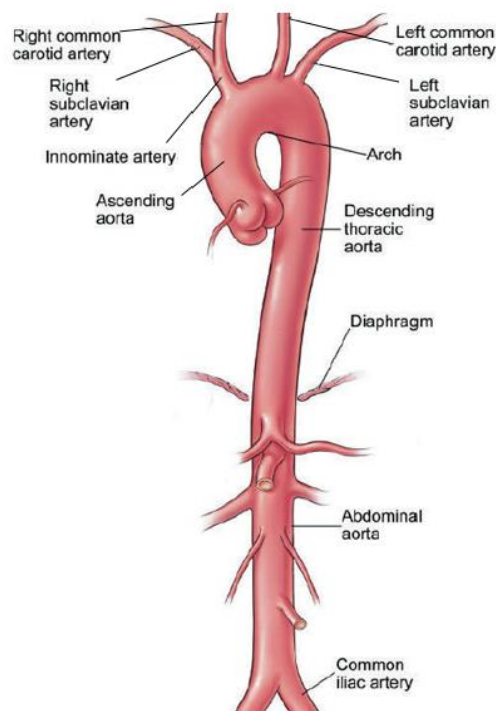


**Figure 1.2:** Anatomy of the human Aorta

## 1.1.4 Blood

Blood tissue consists of a suspension of different particles in an aqueous solution called *Plasma*, which is a slightly alkaline fluid consisting of 90% water and 1% electrolytes. Most of plasma molecules are: globulins, albumin and fibrinogen. The volume percentage of blood particles is called *Hematocrit* (Ht). The hematocrit has a range of 38-52% in healthy men and 36-46% in healthy women, it can be also very high in newborns and in high-altitude populations, while is low in subjects with anemia or thalassemia. The main particles in blood are *Red Cells* or *Erythrocytes*. These cells have no nucleus, a biconcave shape and a diameter of 8  $\mu\text{m}$ ; they are bounded by a membrane called *Stroma*, which is sensitive to mechanical stresses. Very high mechanical stresses cause the rupture of stroma, a phenomenon call *Hemolysis*, or it can undergo an acceleration of the aging process. Red cells are involved in the oxygen transport from the lungs to the tissues. 90% of the protein content in a red cell is made up of *Hemoglobin*, which can reversibly link the oxygen molecules, and this fact increases considerably the amount of oxygen carried into the blood; in fact, without hemoglobin red cells wouldn't be able to sufficiently nourish the organs. Red cells' membrane has a negative charge that, through an electrical repulsion, allows them to maintain a uniform distribution into the vessels. Instead, for low shear rate values of blood flowing, erythrocytes tend to aggregate in rouleaux. This phenomenon is usually observed in microcirculation, in which these aggregates are in the lumen of the vessel and strictly close to the wall to guarantee an efficient release of oxygen and nutrients to the tissues. Other particles that make up the blood are *White Cells* or *Leukocytes*; they occupy some 0.7% of the blood volume in health and they are involved in the immune system. Leukocytes are divided into three groups: *Monocytes*, *Lymphocytes* and *Granulocytes*. These cells have their own nucleus and are produced by the spleen, the lymph nodes and by the marrow bone. The Monocytes are the biggest particles in human blood and are precursors of *Macrophages*, a particular type of cells which can move towards body tissues and are able to engulf and digest other cells or foreign substances like microbes. After maturation, monocytes are released into blood circulation and then they migrate into the connective tissue where become macrophages. Their function is not only phagocytosis, but also secrete defensive substances. Besides, lymphocytes can

recognize and attack invading foreign particles called *Antigens* and help destroy body cells that have become diseased through viruses, infections or cancer. Granulocytes include: *Eosinophils*, *Basophils* and *Neutrophils*. eosinophils attack larger parasites and involved in allergic response, basophils secrete anticoagulants or vasodilators substances, such as histamine and serotonin, and neutrophils contain lysozyme and phagocyte the structure composed of antigen-antibody. Another component of blood particles are the *Plates* or *Thrombocytes*. These cells are spherical with a diameter of 3  $\mu\text{m}$  and they occupy 0.3% of the blood volume in health. Plates are involved in blood clotting and in the repair of damaged endothelium. They can also be activated by increases of wall shear in narrowed vessels. During the hemostasis phenomenon, plates react through three different stages: the adhesion to the damaged endothelium, the activation of receptors and the secretion of chemical messengers and, at last, the aggregation of platelets through receptors bridges. (Figure 1.4)

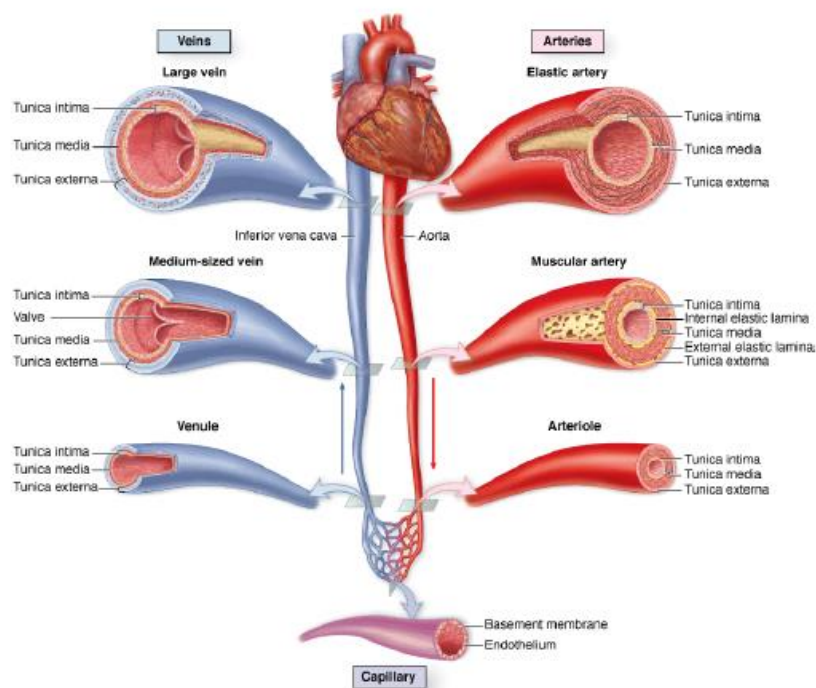


**Figure 1.3:** Representation of blood vessels: large elastic arteries leave the heart and branch to form muscular arteries. These arteries branch further and enter organs, where they branch much further to form arterioles and then capillaries. Blood returns back to the heart through venous system, which increases its diameter by moving from capillaries to large veins

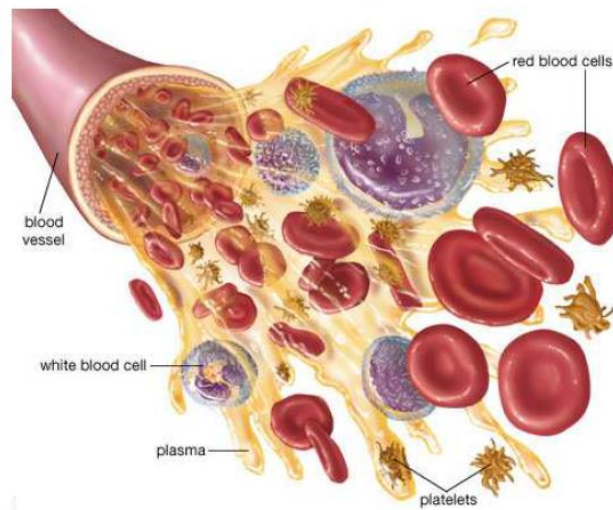


**Figure 1.4:** Representation of main blood particles and plasma.

## 1.2 Aortic Aneurysms

In the most general sense, an aneurysm refers to a focal dilation of a blood vessel compared to its previous diameter or adjacent tissue. If left untreated, aneurysm has the propensity to expand and, eventually, rupture causing severe hemorrhages or, in worst cases, death. Besides, this pathology is characterized by a dramatic decrease of the elastic properties of the aortic tissue. Aortic aneurysms are frequently classified according to morphology or location. Based on morphology, aneurysm can be either *fusiform*, or *saccular*. A fusiform aneurysm is a cylindrical dilatation affecting the entire circumference of the aorta, they have a swelling corresponding to the aneurysmal section of the largest diameter, and a necking referred to the narrow zone between the swelling and the normal aortic tissue. [13] Saccular aneurysms, which are less common than fusiform-types, are outpouchings of the aorta, hence, they don't affect its entire circumference. Aortic aneurysms may also be classified based on their locations as: ascending, aortic arch, thoracic or abdominal. These represent diverse disease processes, and the clinical presentation, natural history and treatment

decisions are different for each segment. [1] Aneurysm development and formation is still not clear, but studies have revealed that are involved local inflammatory responses leading to infiltration of particles such as: macrophages, neutrophils, lymphocytes and a type of connective tissue cells called *Mast cells*. This inflammatory response is further augmented by a great amount of specific proteins, called *Cytokines*, and extracellular proteases enzymes which, in combination, lead to VSMC<sup>1</sup> apoptosis and extracellular matrix degradation. Proinflammatory and anti-inflammatory cytokines control leukocyte recruitment and functions, besides, proteases degrade the peptide bond of elastin and collagen, in the tunica intima, leading to dilatation of the lumen, loss of elasticity and degradation of the aortic wall. (*Figure 1.5 a*) [11] Furthermore, in almost all cases, aneurysmal pathology is predated by the formation of *Atherosclerotic Plaques* which accentuate atrophy of VSMC and of the elastic matrix. These plaques are due to an infiltration, deposition and, finally, oxidation of *Low Density Lipoproteins* (LDL) in the intima layer. (*Figure 1.5 b*) Oxidation is promoted by several factors such as: smoking, hypertension, mellitus diabetes or genetic alterations. Deposition of LDL beckons cytokines and, consequently, leukocytes. As mentioned before, leukocytes include monocytes which are precursors of macrophages. [2] Macrophages phagocyte oxidized LDLs and accumulate lipids in their cytoplasm, this process transforms them into *Foam Cells* which are rich of cholesterol. Macrophages transformation lead to an inflammatory response that keep beckons other macrophages and can move them to apoptosis with the result of calcium deposition into the lipids. Moreover, this process stimulates migration of VSMCs from the tunica media to the tunica intima, and it also produces extracellular matrix, which operate as a scaffold of the growing plaque, called *Atheroma*. The final result is an atherosclerotic plaque formed by a lipid core surrounded by a fibrous cup made of connective tissue.

---

<sup>1</sup> Vascular Smooth Muscle Cells

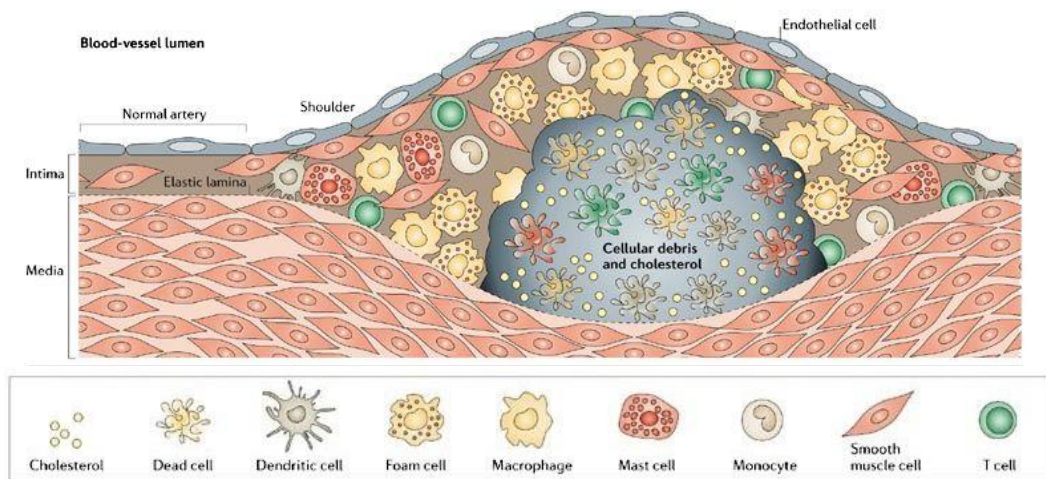


**Figure 1.5 a):** Aneurysm Formation in vessel's lumen

It should be noticed that most of symptoms for both aneurysms and atherosclerotic plaques formation are not noticeable. But when the conditions are very severe the aneurysm tears causing hemorrhage that quickly become fatal and therefore immediately emphasizes the degeneration of this disease. Aneurysm's diameter is the most accepted criterion used to declare its risk of rupture; the threshold value is about 5.5 cm. But, through the years, researchers have discovered that this criterion is not always effective. [15] In fact, there's many other factors, (biomechanical, hemodynamical, and also congenital) that would predict when rupture might occur. For example, there are: wall stresses, the aneurysm's geometry, sex and age of the patient. Anyway, I will later discuss this topic in the section dedicated to the risk of rupture.

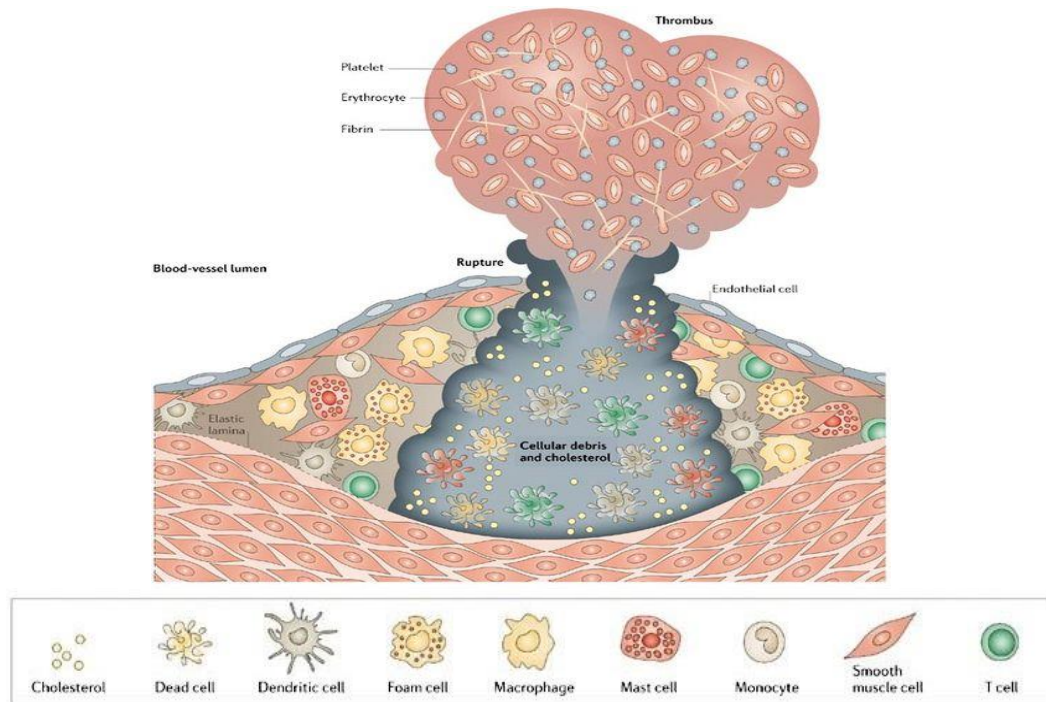


**Figure 1.5 b):** Mechanism of aneurysm rupture and thrombus formation

## 1.2.1 Aneurysms of the Aortic Arch

In this work I've focused on a fusiform aneurysm located between the distal zone of the aortic arch and the proximal zone of the first part of the descending aorta. Moreover, the 3 branches of the aortic arch, the brachiocephalic trunk, the left common carotid artery and the left subclavian artery, were not considered. Supraoptic arteries were disregarded also because the surgical technique for these aneurysms expects endovascular prosthesis for the branches, and we chose to consider only the stent implantation. Aneurysms of the aortic arch may be classified according to the extent of the aneurysm and the surgical repair required. They are common in the proximal arch as the distal-most extension of ascending aortic aneurysms and they become, frequently, fusiform aneurysms which span the entire arch, a minimal part of them present an atherosclerotic ILT (*Intraluminal Thrombus*). Distal arch aneurysms are most commonly atherosclerotic and they can either be limited to the arch itself, or, act as the proximal extent of aneurysms that develops into the descending thoracic aorta. If localized, arch aneurysms are generally saccular and protrude from the

concave surface of the distal arch opposite to the origin of the left carotid and subclavian arteries. Saccular aneurysms may develop *aortic infection*; infections occur when a pathogen offends a vulnerable vessel wall like an existing aneurysm. The infectious agent can either travel through the blood stream and harbor in the vasa vasorum or implant on damaged intima, atherosclerotic plaque or mural thrombus. Leukocytosis and an elevated erythrocyte sedimentation rate can be helpful in indicating the diagnosis but they are not always present. Most arch aneurysms are discovered incidentally as widening of the mediastinum on chest radiography, also they are more symptomatic than aneurysms located elsewhere. Symptoms may include hoarseness, swallowing or respiratory difficulties or superior vena cava obstruction. Three-dimensional Computed Tomography (CT) scanning and magnetic resonance angiograms help delineate the anatomic relation of arch vessels to the aneurysm and can serve as a road map prior to surgical intervention. These less-invasive studies have replaced standard arch arteriography; echocardiography is not ideal for assessing the arch since visualization in this region is inconsistent. Unfortunately, there is very little specific data addressing the risk of rupture for aneurysms of the arch, for this reason data are extrapolated by descending and ascending aortic diseases. It is known that saccular aneurysms have a higher risk of rupture than fusiform-type because of their asymmetry.

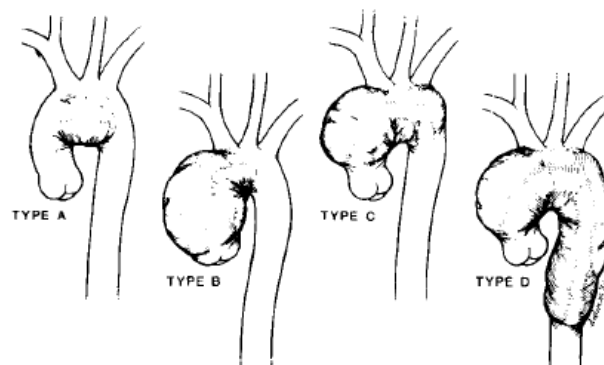


**Figure 1.6:** Classification of aneurysms of the transverse aortic arch based on the extent of the aneurysm and the type of surgical repair

## 1.2.2 Rupture Risk Predictors

The most used aneurysm rupture predictor is diameter, but this criterion allows assessment of the relative rupture risk but not the true individual risk. Studies and trials have concluded that an aneurysm diameter of 5.5 cm should be considered as indication for elective repair in order to prevent its rupture. [12] There is, however, a need for other predictors since aneurysms with a diameter of 5.5 cm continue to grow without rupture, any other may tear before that value. In fact, women have generally smaller vessels, therefore, an aneurysm of a certain size represent a greater relative dilatation of the aorta compared with a same-sized men aneurysm. [35] [34] For this reason, women are inclined to have more advanced disease at the time of treatment. Another important factor, that needs to be considered, is the geometry. When matched for age, gender, and diameter, ruptured aneurysms tend to be less tortuous, yet have greater cross-sectional diameter asymmetry.[8] On conventional two-dimensional CT axial sections, it appears that when diameter asymmetry is associated with low aortic tortuosity, the larger diameter on axial sections more accurately reflects rupture risk, and when diameter asymmetry is associated with moderate or severe aortic tortuosity, the smaller diameter on axial sections more accurately reflects rupture risk. As said before, hypertension, a disease consisting in higher blood pressure than the average, is another factor involved in aneurysm formation and rupture. [24] It's strictly related to wall stress which is considered a more accurate rupture predictor than diameter. In fact, it better differentiates subjects who will have hemorrhages and severe outcome despite their aneurysms diameter is lower than the rupture risk threshold. Wall stress is a more accurate index not only at high pressure analysis, like systolic blood pressure, but also, at a uniform pressure of 120mmHg. A way to reduce wall stresses due to blood pressure might be the presence of a ILT<sup>2</sup>. [7] [25] It works as a damper that reduce the strain, modifying the flow patterns and, eventually, preventing rupture, but only for brief periods of time. Although, long-term presence of ILT is harmful because it alters the normal pattern of oxygen supply to the aneurysms wall. This hypoxic condition may lead to cell dysfunction and extracellular matrix degradation, which may further lead to wall weakening and tear. All these predictors are associated with hemodynamic

---

<sup>2</sup> Intraluminal Thrombus

descriptors which express the pathophysiology of vessel's wall. [26] [33] Most common descriptors are based on the *Wall Shear Stress* (WSS) which is defined as the partial derivative of the velocity parallel to the vessel's wall consider for the distance from the wall coordinate, all multiplied by the blood viscosity. Studies demonstrated that aneurysms zones with a low WSS coincide with zones where rupture occur; anyway, I will discuss this topic later, in the section dedicated to the materials and methods.

## 1.3 Aneurysms Treatments

### 1.3.1 Endovascular Aortic Repair (EVAR)

Endovascular Aortic Repair (EVAR) is a low invasive treatment for aortic aneurysm with a high risk of rupture, located in all the sections of the aorta. It consists of a metallic tubular mesh, called *Stent*, matched to a polymeric porous graft (*Endograft*); [17] it reduces early death, cardiac complications, and length of stay, compared to open surgery. The aneurysmal disease obstructs the vessel and the aim of this device is to reestablish a physiological lumen and a physiological blood flow, acting as an internal scaffold that prevent the wall from tearing. Stents can be made of stainless steel, Co-Cr-Mo alloys (Cobalt Chromium Molybdenum), self-expandable alloys or nitinol, they have also an external film of pyrolytic carbonium, which makes them more hemocompatible. [14] EVAR surgery starts from the left iliac artery, an incision is made and an extra-peritoneal endograft prosthesis is anastomosed to the artery. (*Figure 1.7*) Two catheters are introduced from the orifice: the pig-tail catheter, which is a guide for the angiopathic exams, and the rigid catheter, which is the guide for the endograft-releasing system, it has a flexible conical tip connected to a balloon, that will then be used to expand the endograft. The endograft-releasing system consist of a small tube in which the graft is folded by a thin casing, at the most proximal part of the tube is settled a mechanism that lets the graft flows through the guide and at the same time gradually makes the graft expands. Once the

stent it's totally deployed in the target zone of the artery, the balloon is inflated making the distal part and the proximal part of the prosthesis adhere to the wall's vessel and the catheters are removed. Generally, grafts are inserted 1-3 cm upper to the zone of interest to prevent stent migration during the expansion, and let the stent's position to be adjusted while is partially opened.

There are many different types of graft depending on surgery techniques or disease zones; usually grafts are patient-specific, designed on the geometric features of the patient's vessels, this process may require several weeks. [21] Grafts may present branches and/or fenestration, and being made of different polymers. The most used is *Dacron*®, the commercial name of polyethylene terephthalate, which can have different sewing wefts. Another polymer is *Teflon*® polytetrafluorethylene (PTFE), which can be both used as sewed or as expanded, named *Gore-Tex*®. Less-used are the polyurethane ones, which have the advantage of a pour-variable design. Moreover, to improve intraluminal endothelialization, stent-grafts may be loaded with heparin.

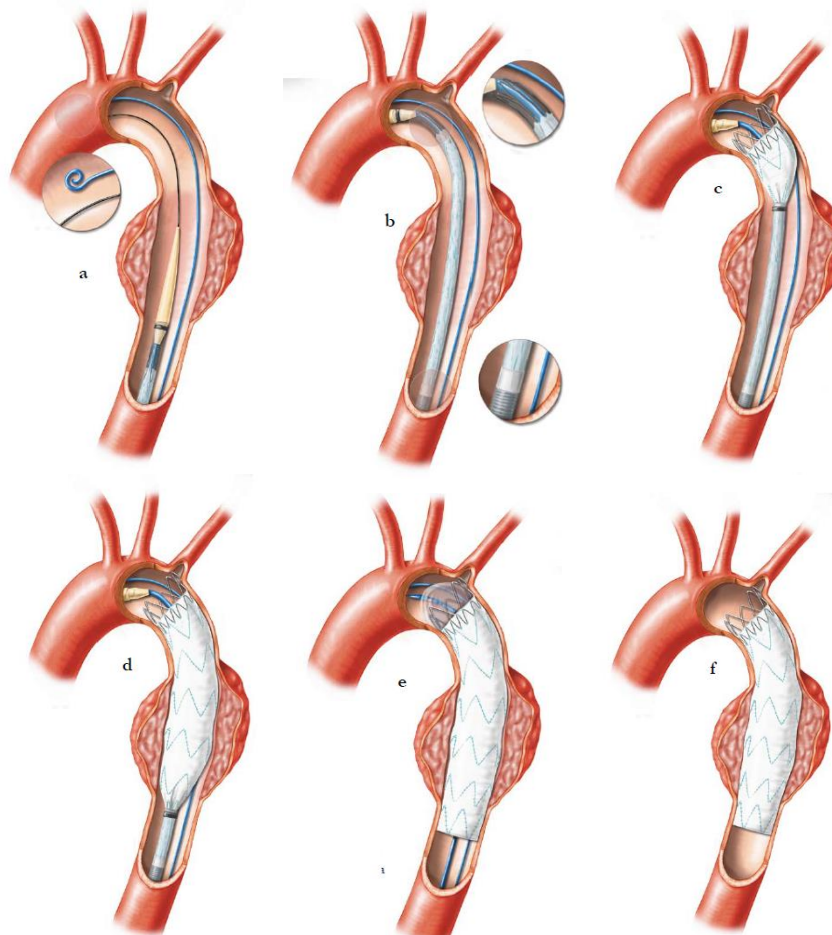


**Figure 1.7:** EVAR implantation technique: a) catheters introduction b) conical tip tube introduction c) and d) graft deployment e) balloon expansion f) EVAR's position adjustment

## 1.3.2 Flow-diverting Stents (FDSs)

The deployment of fenestrated and branched stent grafts may be complicated, because of anatomical factors, and, sometimes, technically challenging. Moreover, a patient-specific fenestrated stent graft requires from 6 to 8 weeks to manufacture which precludes its application in emergency cases because the waiting time exposes patients to risk of aneurysm rupture as well. Flow-diverting stents represent an effective option which solve these problems. FDSs are usually used for cerebral or intracranial aneurysms, but recently they showed satisfactory results also in peripheral aneurysms. These devices are specially designed to reduce flow velocity in the aneurysm sac and promote thrombosis while maintaining flow in the main artery and branch vessels. To understand the mechanism by which an FDS can cause thrombosis, the hemodynamics within the aneurysmal sac must be studied first. For an aneurysm without collaterals, blood flowing into the sac generates vortices. As these flow perturbations progress, they become stronger until they reach the aneurysm outlet, and these continuous movements induce stresses to the arterial wall. [9] FDSs include: The Pipeline Embolization Device (PED), the SILK® Fluid Diverter (SFD) device and the Multilayer Stent. The PED is a self-expanding, microcatheter-delivered device made of platinum and a cobalt-nickel alloy and it provides an area of coverage three times bigger than EVAR devices. The PED is attached to a pusher wire, which has a coil tip beyond the distal part of the device; once positioned across the aneurysm, the delivery wire is held and PED is carefully unsheathed. Once the unsheathed segment begins to expand, the distal end is released by clockwise rotation of the delivery wire. The proximal segment of the PED can then be deployed, through the application of forward pressure on the delivery wire, supplemented by unsheathing. SILK® is a flexible, self-expanding device consisting of a braided mesh cylinder with flared ends. Insertion technique involves deploying the distal tip of a delivery microcatheter to the aneurysm and then pushing the SFD to the tip of the delivery wire to which it is attached. The system is then aligned with the aneurysm, and

the SFD is deployed by unsheathing it from the constraint of the microcatheter. This involves a combination of pushing the delivery wire and retrieving the microcatheter to allow the SFD to expand and to compensate for any resulting foreshortening. SILK® acts as a barrier on the aneurysm neck reducing its flow velocity and WSS and increasing the contrast material washout time. The Multilayer Stent is a tubular, self-expanding stent consisting of multilayer braided wires made of a cobalt alloy, and it's available in different diameters. As for EVAR treatment, the stent is deployed through a radiopaque guiding catheter, access is preferentially from the femoral artery. When the deployment site is reached, the top of the delivery system is placed a few centimeters above and the metallic pusher is slowly pushed with the sheath fixed under radioscopy, and the multilayer stent begins to be released. After full stent deployment, the pusher is pulled back in its initial position so that the tip comes in front of the outer sheath; finally, the delivery system is removed. [10] When an FDS is placed in the aneurysm, stent geometry reduces the flow velocity within the aneurysm vortex while improving laminar flow in the main artery. [16] Aneurysm's thrombosis, generated by these devices, is followed by sealing of the luminal surface by a layer of neointimal tissue, which will consequently lead to cicatrizes and reverse remodeling of the aneurysm.

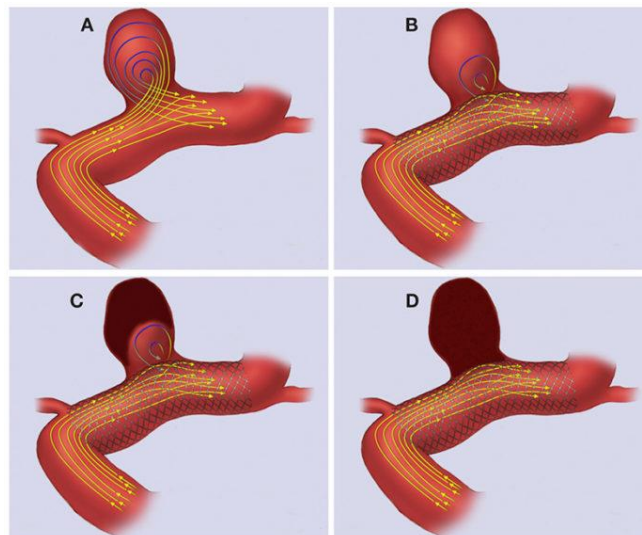


**Figure 1.8:** Aneurysm's flow velocity reduction with a FDS

### **1.3.3 Multiple Overlapping Uncovered Stents (MOUS)**

These devices are usually involved with the treatment of complex aortic aneurysm involving side branches. MOUS may be used as stand-alone devices or they may represent an alternative to multilayer stent in flow-diverting devices. In fact, multilayer stents are highly deformable, may exhibit fore shortening during deployment, and they may be undersized; all these complications could lead to inadequate aneurysm coverage and device migration. MOUS consist in multiple uncovered or multiple bare metal stents made by self-expanding alloys like stainless steel or nitinol. Stent cells have many different designs, they are connected at the midpoint of the longest curved segments to create elastic joint that increase the overall stent flexibility and to allow zero shortening upon expansion, preserving the original stent length. Every single cell is composed by curve elements with variable sections to improve mechanical behavior for expansion, flexure and torsion solicitations. The devices may present from 1 to 4 stents overlapped, and, as FDSs, promote development of thrombus by modulating local flow pattern that reduce wall tension, while maintaining patency of side branches. [3] [4] Despite stress levels in the aneurysm zone decrease, MOUS may present undesirable effects around the landing zone, inducing elevated stress concentration that intensify with the number of stent overlapped. Besides, the formation of thrombus might not be always protective in the long term. As said before, inflammatory content might infiltrate the aneurysm wall beneath thrombus and thick thrombus might lead to local hypoxia and neovascularization. [5] The implantation procedure starts, generally, from the femoral artery, which is exposed and supplied with heparin. Then an angiogram is performed through a pig-tail catheter, which confirms the aneurysm location. A stiff wire is then placed across the lesion segment, and through this wire, the stent is advanced and deployed, from proximal to distal zone, to cover the aneurysm. The deployment is performed with a lesion free-landing zone of almost 10mm at both proximal and distal neck, to prevent migration. [6] The number of uncovered stents implanted is determined by intraoperative angiography with the criterion that a decrease of velocity in the aneurysmal sac was achieved on fluoroscopy. Also, side branches are covered whenever necessary.

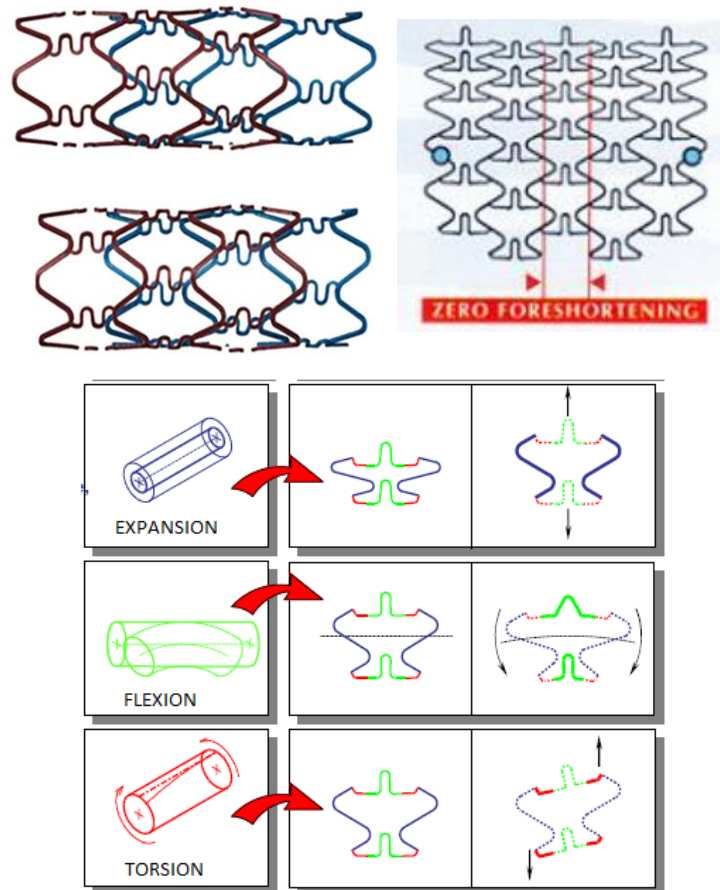


**Figure 1.9:** Examples of MOUS conformation and cell's properties

### 1.3.4 Treatment's Failure: Endoleak

In EVAR and FDS implantations may occur a shortcoming called *Endoleak*, consisting in blood persistence in the aneurysm sac even though the presence of a prosthesis, which is supposed to exclude aneurysm from blood circulation. Endoleak may be classified basing on causes:

- *Type I*: consisting in blood flowing between the stent and native vascular system, it may be subdivided in *Type I-a*, if flowing occurs in the proximal zone of the prosthesis, and, *Type I-b*, if flowing occurs in the distal zone.

- *Type II*: consisting in back-flow in the aneurysm sac becoming form other arterial branches
- *Type III*: due to manufacturing shortcomings or cells disconnection
- *Type IV*: due to a continuous dripping through stent's porosity
- *Type V*: also known as *Endotension*, consisting in the continuous dilation of the aneurysm lumen without an indication of leaking, in this case the cause is the pressure not the flow.

During implantation, a solution to prevent this problem may consists in: better graft alignment, introducing an additional stent or re-expanding the graft with the balloon. As for branched stent-grafts, by-passing arterial branches may represent a solution that will help revascularization. As for FDSs, a solution to this problem may be an intra-operative sac embolization. [18] Endoleaks are highly correlated with the peak systematic blood pressure and the local stress along the interface between a stent-graft and the aneurysm sac. The early detection of endoleaks may reduce the risk of failure and delay aneurysm propagation.

### **1.3.5 Treatment's Failure: Migration**

Migration usually consists in distal movement of the proximal portion of the stent. [31] It may be thought of as a failure of attachment with an overregulated aorta or as a failure related to changes in aneurysm morphology. Factors that help maintain stent-graft position include: friction, barb or hook penetration, column strength and arterial ingrowth. [19] Hooks and barbs may increase the fixation but they can also cause complications in case of diseased aortic necks. It has also been found the advantage of oversizing prothesis and that sufficient anchorage is achieved in an aortic neck of 10 mm to prevent migration when the stent-graft is fully deployed. Moreover, blood flow friction generates drag forces on the prothesis that disturb the fixation e may cause migration.

## 1.4 Aim of the Study

Multiple overlapping uncovered stents (MOUS) system have shown potentials in managing complex aortic aneurysms. They promote the development of thrombus by modulating local flow pattern that reduces the wall tension and reduce risk of rupture. In my work I've considered one stent of a three-component MOUS device, and I've tested its validity in three different aortic models with the same sized fusiform aneurysm. The purpose was to test the stent efficacy in different aortic zones, both straight and curved. The first two models were idealized, with opposite geometrical conditions, the third model has been projected basing on real clinical aortic image. The first model was straight tubular, besides, the second was curved with the inlet and outlet surfaces depicted on perpendicular planes. In the second model, fusiform-type aneurysm was placed between the proximal and the distal zone of the curve and in the patient-specific model, between the distal zone of the aortic arch and the proximal zone of the first part of the descending aorta. In this model the 3 supra-aortic branches were not considered to make the model more accurate for the comparison with the other two. A computational hemodynamic analysis was performed to extrapolate flow descriptors that would predict where the maximum-stressed zone was. Every model was simulated with and without the stent inside in order to evaluate stent's efficacy. We would expect a minor stress and a major particles deposition in the stented models.

# Chapter 2

## Materials and Methods

In this chapter I report the geometrical characteristics of aortic and stent models. Then, the computational mesh method, considering solution accuracy and memory cost. Subsequently, the sensitivity analysis of steady-state simulation, used as choice criterion for unsteady-state simulations, are described. Finally, methods used to perform post-processing analysis are discussed.

## 2.1 Aortic Models with Aneurysm

Three different aortic models were created. The first two were totally idealized and created using Solidworks® software only. The third one has been projected basing on real clinical aortic image, and using two different software: vmtk and Solidworks®. The first model was straight tubular with a diameter of 19.90 mm and a length of 310 mm, with a fusiform-type aneurysm located in the center. The aneurysm had a symmetric elliptical shape made up of two loft solid extrusions, with a longitudinal length of 70 mm and a diameter of 40 mm. The second model was tubular curved with the inlet and the outlet surfaces depicted on perpendicular planes, in its complex it had a fourth-part of circumference shape with an arc length of 310 mm. The aneurysm geometry was the same of the previous model and located as well at the center of the arch.

The third model was patient-specific and created from a clinical image of a healthy human aorta. At first, with vmtk software, the supraortic branches were cut out in order to have a more accurate comparison with the other two models. Then the *centerline*, which is the line equidistant from all the vessel's surfaces, was created. These data were then imported into Solidworks® software to create the geometric model of the aorta without the brachiocephalic trunk, the left common carotid artery and the left subclavian artery. To figure out the dimensions of the arch and the length of the ascending zone, other measures were performed with the clinical image. The result was a tubular shape model with a hairpin turn in the proximal zone. The aneurysm had the same dimensions of the other two models and was located between the distal zone of the aortic arch and the proximal zone of the first part of the descending aorta. But, in this case, it was designed with a more accentuated swelling in the concave part of the arch to have a more physiological shape. In fact, in this zone fusiform-type aneurysm are less common; the growth of the aneurysmal sac seems to follow the blood flow, creating an outpunching that, in most cases, doesn't occur in the convex zone. To recreate this situation, the fusiform-type aneurysm was asymmetric in the model. The entire length, including ascending, arch and thoracic zone, was 300 mm and the diameter was 19.90 mm. All models were symmetrical to, at least, one plane so they were all sectioned in their symmetric axes. The first model was symmetrical to the Right Plane and to the Superior

Plane and was sectioned two times. The other two models had just one plane of symmetry, and they were sectioned in the Right Plane and in the Frontal Plane, respectively. These cuts were performed to reduce computational times and memory costs.

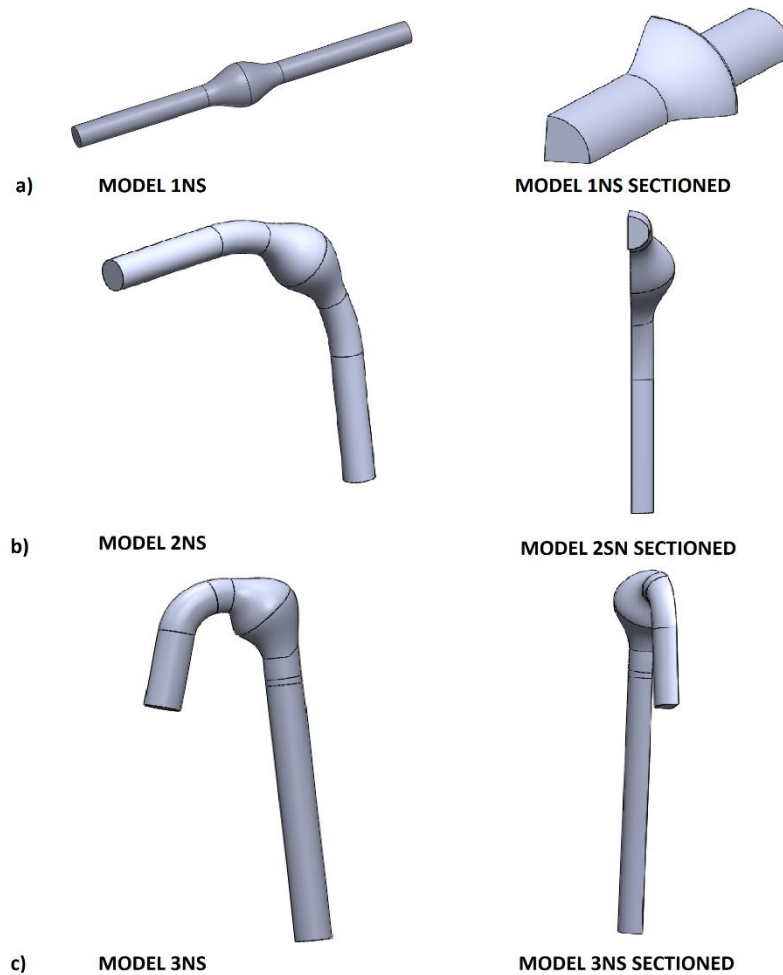


**Figure 2.1:** Aortic models full and sectioned: a) model 1NS b) model 2NS c) model 3NS

## 2.2 Stent Models

The stent as well was created in Solidworks®. It started from 20 squares with a side of 0.13 mm depicted, at 18° one from another, on a circle with a

diameter of 19.87 mm. Then they were simultaneously extruded and rotated for two cycles, following, as direction, a guide-line which coincided with the centerline of every model. The shape of the guide-line varied in the three models, but its length was set at 15 mm. Stent cells were very flexible so that their geometry could vary whereas curvatures occurred. In the first model, which had a straight-shape guide-line, all the stent cells were geometrically identical, consisting in a quadrilateral 2.3x2.28 mm sized. For the second model the centerline was a fourth-part of circumference arch; for this reason, the cells had a smaller size from the first ones (2.2x2.2 mm) and they maintained their size as well in all the stent zones. In the third model the guide-line coincided with the centerline of the aorta. In this case the cells dimensions varied through all the stent geometry, which was the most changeable. In particular, the most noticeable difference in cells dimensions was between the intrados zone and the extrados zone of the aortic arch. In the intrados, the smaller cell had a dimension of 1.88x1.89 mm whereas, in the extrados zone, the biggest cell had a dimension of 2.10x2.50 mm. Finally, stent models were implanted in aortic models and they were sectioned as well. (Figure 2.2)

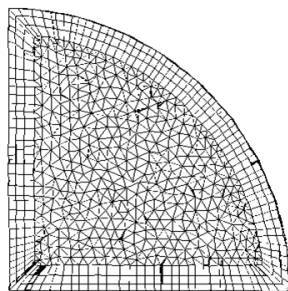


**Figure 2.2:** Stent models and final model made of aortic model and stent, in the last column they are illustrated as sections: a) model 1S b) model 2S c) model 3S

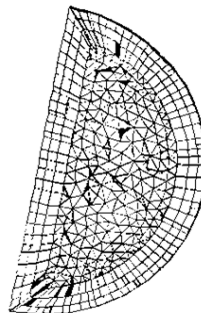
## 2.3 Computational Mesh

Finite element analysis and models' discretization were performed with ANSYS ICEM® CFD software. Hybrid grids were generated for each model, with and without the stent. All "Unstented" meshes had the external shell and the core made of tetrahedral elements, whereas, the boundary layer region was made of prismatic elements. (Figure 2.3 a)) It should be noticed that the prismatic layer laid, also, in the cutting-zone of the vessel's lumen. In the next step, when the specular symmetric zone of the models has been created, this layer has been built as well, with the result of having a boundary layer in the center of the lumen. Anyway, this fact hasn't influenced the final outcome. As for "Stented" meshes, the boundary layer wasn't prismatic but tetrahedral and it was thinner than the unstented grids. This layer was created to have a better resolution near the vessel's wall zone. (Figure 2.3 b)) Meshing method consisted, firstly, in a Robust (Octree) method which generated a tetrahedral/mixed surface mesh and, secondly, in a Quick (Delaunay) method which generated the definitive volume mesh. Four meshes per model were performed, differing from each other's in number of elements and accuracy. *Maximum element size, smaller element size, refinement and ortho weight* were the parameters modified in each model's mesh to improve geometry reconstruction and element subdivision. After every mesh method, a smoothing option was applied to have a better mesh quality and to not have disturbance with the next phases. Smoothing was performed with a high number of iteration, from 70 to 120 for the Robust method, and, from 5 to 20 for the Quick method. In this case a level of quality equal or greater than 0.3 was considered as "good".

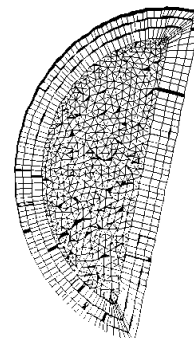
a) Model 1NS

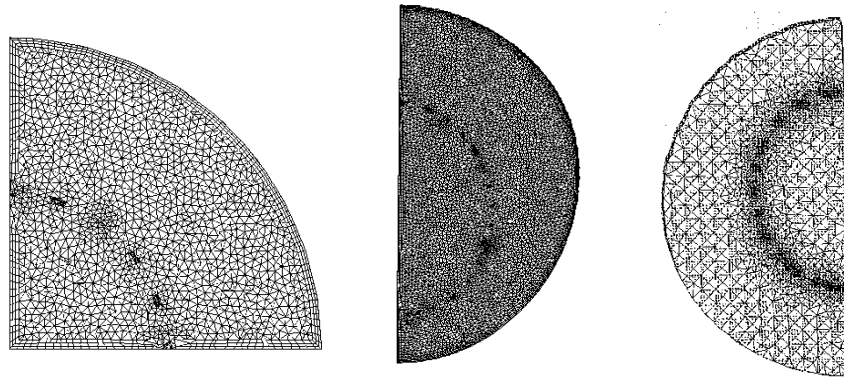


Model 2NS



Model 3NS





**b) Model 1S**

**Model 2S**

**Model 3S**

**Figure 2.3 a):** Meshes' bodies for Unstented models 1NS 2NS 3NS

**Figure 2.3 b):** Meshes' bodies for Stented models 1S 2S 3S, the holes in the body are due the stent implantation

## 2.3.1 Mesh Sensitivity: Steady-State Simulations

In the next step, a mesh sensitivity has been conducted in order to make results of numerical analysis grid-independent. Steady-state simulation parameters are reported below:

- Steady-state flow condition
- Blood was considered a Newtonian fluid with density equal to  $1,060 \text{ Kg/m}^3$  and viscosity equal to  $0.0035 \text{ Pa}\cdot\text{s}$  or  $35 \text{ cP}$ .
- *Boundary Conditions:* flat-profile velocity equal to  $0.2 \text{ m/s}$  set in inlet, this value was calculated from the geometry and the flowrate. No-slip flow condition at vessel's wall and Relative Pressure equal to  $0 \text{ Pa}$ .
- Residual set to  $10^{-4}$  as convergence criterion
- To control numerical simulation, volume flowrate at inlets and outlets have been monitored

- The motion variables were initialized at 0 and the number of maximum iteration was set to 1100. Data were acquired at every iteration

## 2.3.2 Mesh Sensitivity Analysis

In this analysis four different grids per model, with increasing number of elements, were created. The fourth grid was the most accurate and the one with the maximum number of elements. The number of prismatic layers in the boundary was set to 3 for every grid. The following parameters have been analyzed:

- Volume Averaged Velocity
- Maximum Velocity
- Mean Wall Shear Stress
- Maximum Wall Shear Stress
- Minimum Wall Shear Stress

Percentage differences of these parameters were then performed, considering the densest mesh as landmark. Minimum and Maximum WSS were the most variable parameters and, for that reason, they were taken as second criterion of choice to establish which grid would better represent that specific model. The most predictive parameters were the mean velocity and the mean WSS; also, the number of elements, meant as computational time and data storage, were considered. Differences had to be equal or lower than 1% to be accepted. For the first two unstented models was chosen the grid number one (with 163,192 and 638,020 elements respectively) and, for the third unstented model and the first stented model, the grid number three was chosen (with 1,952,953 and 4,186,587 elements respectively). (*Figure 2.4*)

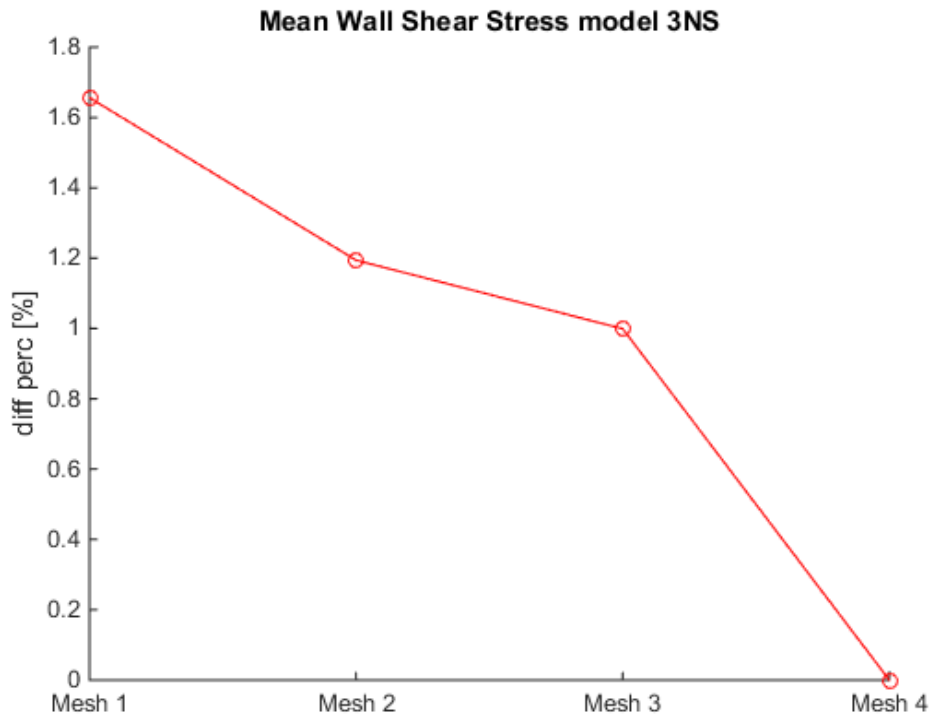


**Figure 2.4:** Example of sensitivity analysis of model 3NS, different percentages of Mean WSS are illustrated

Model 3 NS	MESH 1	MESH 2	MESH 3	MESH 4
<b>NODES</b>	145,483	286,641	528,436	928,932
<b>ELEMENTS</b>	565,218	1,114,058	2,258,470	3,997,578
<b>VOL. AV. VELOCITY [m/s]</b>	0.1759195	0.1759079	0.1756651	0.1755673
<b>MAXIMUM VELOCITY [m/s]</b>	0.2990325	0.3029342	0.3084572	0.860085
<b>MEAN WSS [Pa]</b>	0.6895623	0.69280308	0.6941693	0.7011755
<b>MAXIMUM WSS [Pa]</b>	5.070643	5.049613	6.108209	6.180238
<b>MINIMUM WSS [Pa]</b>	0.01175593	0.006155	0.0129414	0.0068002

**Table 1:** Example of mesh sensitivity for model 3NS. Number of nodes and elements for every grid, then values of sensitivity parameters are reported

## 2.4 Unsteady-State Simulations

The next step consisted in computational fluid dynamics, performed with the finite volume package ANSYS Fluent® v.6 After simulations mean and peak velocity data, dynamic and static pressure data, WSS data and helicity data have been extracted

### 2.4.1 Governing Equations

The fluid dynamics can be described through the conservation laws, in terms of the conservation mass, momentum and energy, along with the continuity equation. To study the fluid flow in a three-dimensional domain, two different methods are used: the *Eulerian approach* and the *Lagrangian approach*. In the first method, physical and thermodynamics variations are described for fixed space references of the domain, whereas, the Lagrangian approach, describes fluid dynamics throughout the conditions of the fluid particles in a specific time-set. For this study, an Eulerian approach was adopted.

The continuity equation states that the incremental mass rate, in a control volume  $dx dy dz$ , is due to the incremental rates of the fluid flow through the volume surfaces. (Equation 2.1)

$$\frac{\partial \rho}{\partial t} = - \frac{\partial \rho u_x}{\partial x} - \frac{\partial \rho u_y}{\partial y} - \frac{\partial \rho u_z}{\partial z} \quad (2.1)$$

where  $u$  is the fluid velocity and  $\rho$  is the density

Considering the fluid as incompressible,  $\rho$  is a constant and we obtain

$$\rho = \rho(t, x, y, z) \quad (2.2)$$

$$\nabla u = 0 \quad (2.3)$$

The momentum conservation law states that the incremental rate of the momentum in a control volume  $dx dy dz$  is due to the sum of:

- the difference between incoming and outgoing flowrate
- the external forces operating on the volume surfaces
- the internal volume forces, like the gravity

Adopting the assumption of incompressible fluid, the momentum law may be also being written as

$$\rho \frac{Du}{Dt} = -\nabla P + \mu \nabla^2 u + \rho g \quad (2.4)$$

Which is known as the *Navier-Stokes* equation, where  $u$  is the velocity vector in the three space dimensions  $xyz$ ,  $P$  is the static pressure,  $\mu$  is the fluid viscosity,  $g$  is the gravity vector in three space dimensions and  $\frac{Du}{Dt}$  is the Substantial Derivate which can be written as

$$\frac{Du}{Dt} = \left( \frac{\partial u}{\partial t} + u \nabla u \right) \quad (2.5)$$

## 2.4.2 Computational Settings and Boundary Conditions

The blood was assumed as a homogeneous, incompressible Newtonian fluid. Its dynamic viscosity was set equal to 0.0035 Pa\*s or 35 cP and its density to 1,060  $Kg/m^3$ . The simulations' technique started from a set inlet flow-rate wave-form which assigns, to the velocity inlet, its corresponding time step,

calculating the models surface from the grids. (Figure 2.5) Time steps were set to a number of 1,100. Flowrate was set to a lower value to not have a turbulent regime. The flow was supposed unsteady, No-slip flow condition at vessel's wall and Relative Pressure equal to 0 Pa were considered as boundary condition. The residual criterion to ensure convergence was set to  $10^{-4}$  for a cycle of 1.1 s with time-steps of 1ms. To eliminate the start-up effects of transient flow, at every iteration, a residual equal to 2,000 must be reached. From one and half to two cardiac cycles have been simulated and the second period result was taken into account. For every cycle, one time step in two has been considered in order to eliminate memory cost. To establish simulations convergence, different percentages of volume average velocity and mean WSS of same time-steps form different cycles have been evaluated, this difference must be lower than 1%.

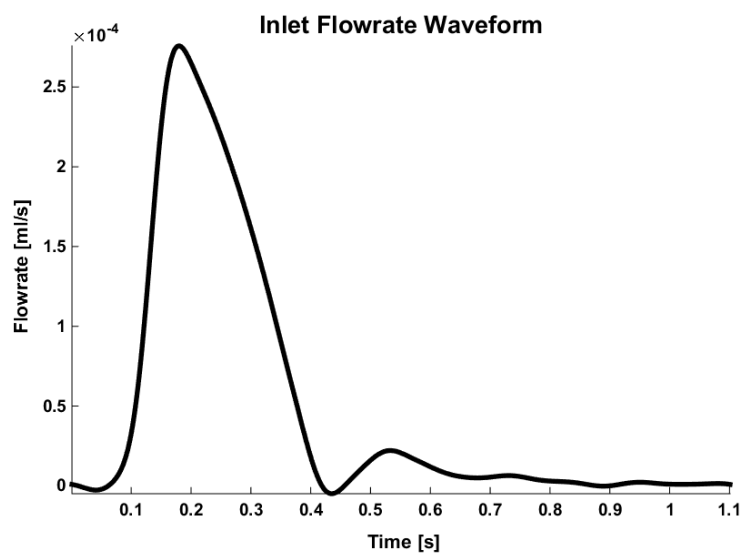


Figure 2.5: Inlet flowrate waveform

## 2.5 Post-Processing Analysis

In this final step, WSS and Helicity data have been computed with MATLAB® (the Mat-works) software and visualized with Tecplot 360® (v. 2009).

## 2.5.1 Wall Shear Stress (WSS)

Hemodynamic forces, acting on the vessel wall, are fundamental in maintaining the normal functioning of the circulatory system because arteries adapt to long term variations in these forces. In the presence of increased forces magnitude, arteries tend to dilate and remodel to a larger diameter, while, in the presence of decreased forces magnitude, they tend to shrink and remodel to a smaller diameter. This adaptation process is mostly due to a hemodynamic factor called Wall Shear Stress (WSS). Considering a fluid flowing in a cylindrical tube, its velocity varies along the radius of the conduit. Velocity profile has a parabolic-shape, it has a maximum at the center of the tube and decreases toward the walls. Fluid viscosity exerts frictional forces between adjacent layers of the flowing fluid, and, between the fluid and the tube wall; through these aspects, frictional forces generate a velocity gradient in the conduit. Wall Shear Stress is defined as the force per unit area created when a tangential force acts on a surface, in this case, blood flow represents the tangential force and, endothelium represents the surface. (Figure 2.6)

The magnitude of WSS is proportional to the velocity gradient near the conduit wall, which is called *Wall Shear Rate* (Equation 2.6)

$$WSS = \mu \left( \frac{\partial u}{\partial t} \right)_{y=0} \quad (2.6)$$

where  $y$  is the distance from wall,  $u$  is the fluid velocity and  $\mu$  its dynamic viscosity. WSS is measured in  $Pa$  or  $dyne/cm^2$  ( $1 Pa = 10 dyne/cm^2$ ). WSS can change the morphology and the orientation of the endothelial cell layer. Laminar flow with high WSS tend to elongate these cells and to align them in the direction of the flow, whereas, low or oscillatory WSS tend to desegregate cells and doesn't make them have a clear orientation.

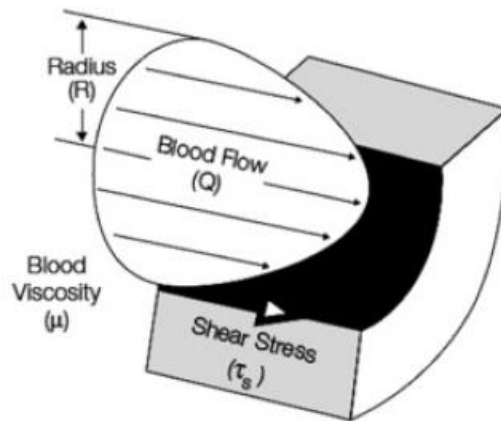


**Figure 2.6:** Velocity distribution and WSS in a lumen vessel

## 2.5.2 WSS-Based Predictors

In order to predict variation of wall shear stress during a cardiac cycle, Computational Fluid Dynamics (CFD) calculates WSS values for each node of discretized vessel wall at each cycle. The parameters suggested to synthesize information derived from CFD analysis, known as WSS-Based predictors, are reported below.

### ***Time-Averaged Wall Shear Stress (TAWSS)***

TAWSS indicates the average of WSS in a time-period T. Time-Averaged Wall Shear Stress was calculated by integrating each nodal WSS vector magnitude at the luminal surface over the cardiac cycle.

$$TAWSS = \frac{1}{T} \int_0^T |WSS(s, t)| dt \quad (2.7)$$

It is widely accepted that TAWSS values lower than 0.4 Pa stimulate a pro-atherogenic endothelial phenotype, while, TAWSS values between 1.5 and 10-15

Pa induce quiescence and athero-protective gene expression profile. Higher TAWSS values, greater than 15 Pa, can lead to endothelial trauma.

## ***Oscillatory Shear Index (OSI)***

OSI is used to identify regions on the vessel wall subjected to high oscillatory WSS values during a cardiac cycle.

$$OSI = 0.5 \left[ 1 - \left( \frac{|\int_0^T WSS(s, t) dt|}{\int_0^T |WSS(s, t)| dt} \right) \right] \quad (2.8)$$

Oscillatory Shear Index is an adimensional number included between 0 and 0.5. When OSI=0 it means that flow is unidirectional and that WSS never changes direction. An OSI=0.5 corresponds to a highly disrupted flow where WSS doesn't follow a preferential direction. Therefore, zones with OSI near to 0.5 attend to be more pro-atherogenic, whereas, vessel zone with OSI near to 0 attend to be more athero-protective.

## ***Relative Residence Time (RRT)***

RRT is combination of TAWSS vector and OSI

$$RRT = \frac{1}{(1 - 2 \cdot OSI)TAWSS} = \frac{T}{|\int_0^T WSS(s, t) dt|} \quad (2.9)$$

This parameter attends to find zones with both high OSI and low TAWSS, but is not a robust predictor of low and oscillatory shear index. If TAWSS is low, RRT

increase independently from OSI. That because TAWSS and OSI have different ranges, between 0 and  $\infty$  and between 0 and 0.5, respectively.

### 2.5.3 Helicity

In this section the relationships between bulk flow and development of arterial disease are discussed. An arrangement of this type of flow progression in complex vortical patterns might play a significant role in the tuning of the intima's cells and blood vessel-wall interactions. Moreover, bulky-flow structures are primarily responsible for mass transfer, in particular, for those blood particles that take advantage of mixing induced by convection. A better understanding of the role of pitch and torsion in blood flow development can be obtained through *helicity*, which is related to the reduction and redistribution of energy through various scales.

*Density of Kinetic Helicity*  $h$  is the product between velocity  $\mathbf{v}$  and the curl of the velocity vector

$$h(s; t) = \mathbf{v} \cdot (\nabla \times \mathbf{v}) \quad (2.10)$$

The curl of the velocity vector is also called *Vorticity*  $\omega$  and its formulation is reported below

$$\omega = (\nabla \times \mathbf{v}) = \begin{bmatrix} \hat{i} & \hat{j} & \hat{k} \\ \frac{\partial}{\partial x} & \frac{\partial}{\partial y} & \frac{\partial}{\partial z} \\ u & v & z \end{bmatrix} \quad (2.11)$$

Vorticity vector measures the spin of the fluid element and detects its direction. The spin is due to a combination of a rotational component and a translational component that form an helicoidal-shape motion. Particles direction depends on

the angle between the components,  $\varphi$ , as the result of a scalar product. For this reason (Figure 2.7), the helicity equation may also be written as

$$h = \mathbf{v} \cdot \boldsymbol{\omega} = |\mathbf{v}||\boldsymbol{\omega}|\cos(\varphi) \quad (2.12)$$

$h$  is a scalar value and a measure of the vorticity and the velocity vectors alignment. When  $\varphi = 90^\circ$  the two vectors are perpendicular and the helicity is null,  $h=0$ . When  $\varphi = 0^\circ$  or  $\varphi = 180^\circ$  the vectors are aligned and the spin is counterclockwise or clockwise respectively.

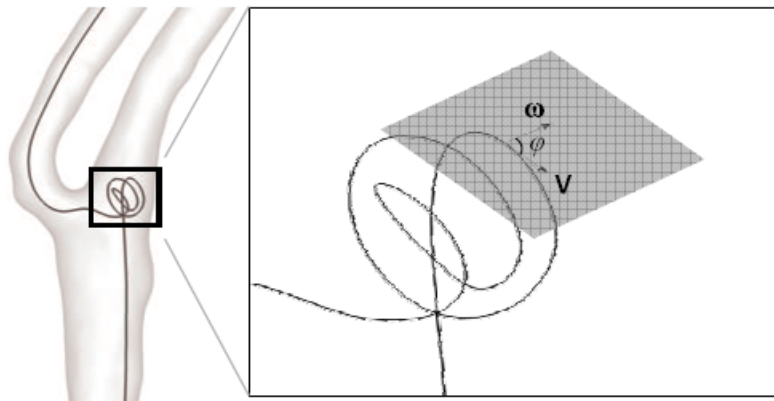


Figure 2.7: Helicity representation

## 2.5.4 Helicity-Based Descriptors

### *Local Normalized Helicity (LNH)*

LNH is used to have a time-mapping of the fluid particles trajectory and velocity. It is useful to deduce if there are one or two counter-rotating structures in the vessel. Local normalized helicity consists in the density of helicity normalized

to the velocity and vorticity vectors modules, which corresponds to the local angle between the above-mentioned vectors.

$$LNH = \frac{\mathbf{v}(s; t) \cdot \boldsymbol{\omega}(s; t)}{|\mathbf{v}(s; t)| \cdot |\boldsymbol{\omega}(s; t)|} = \cos\varphi \quad (2.13)$$

LNH varies from -1 to 1; a negative sign denotes a clockwise rotation of the fluid domain structures, while, positive sign denotes a counterclockwise one. When LNH is equal to  $\pm 1$  the flow is exclusively helical, while, if it is equal to 0 a symmetry of helical structures occurs.

## ***Quantitative Helicity Indexes***

Quantitative helicity indexes were firstly proposed by Gallo et al [32].; they attempt to describe helical flow structures in terms of strength, size and relative rotational direction. They are in number of 6 denoted with  $h_1 \dots h_6$ , and their formulation are reported below.

$$h_1 = \frac{1}{TV} \int_T \int_V H_k dVdt \quad (2.14)$$

$$h_2 = \frac{1}{TV} \int_T \int_V |H_k| dVdt \quad (2.15)$$

$$h_3 = \frac{h_1}{h_2} \quad (2.16)$$

$$h_4 = |h_3| = \frac{|h_1|}{h_2} \quad (2.17)$$

$$h_5 = \frac{V_d}{V_m} = \frac{\int_T \int_{V_d} dV dt}{\int_T \int_{V_m} dV dt} = \frac{\max(V_+, V_-)}{\min(V_+, V_-)} \quad (2.18)$$

$$h_6 = \frac{\frac{1}{V_d} \int_T \int_{V_d} H_k dV dt}{\frac{1}{V_m} \int_T \int_{V_m} H_k dV dt} \quad (2.19)$$

Where  $T$  is the time-period of the cardiac cycle,  $V$  is the fluid volume,  $V_+$  and  $V_-$  are the total volumes of the helical structures rotating in clockwise verse (positive) and counterclockwise (negative) verse.  $V_d$  and  $V_m$  are the volumes occupied by the dominant and the minor direction of helical structures rotation, respectively.  $H_k$  is the helicity. The descriptor  $h_1$  consists in the *Time Averaged Helicity* normalized to the integration volume, if  $h_1 = 0$  there are symmetric counter-rotating helical structures in the domain, or no helicity occurs. If it has a signed value, its sign indicates that the rotation has a clockwise verse or a counterclockwise verse. The descriptor  $h_2$  is given by the integration of the helicity modulus and it indicates the total amount of the helical flow in the domain, so, it doesn't consider the direction of the rotation of the fluid structures. The  $h_3$  descriptor consists in the ratio between the two previous indexes and, for this reason, is a adimensional value which varies from -1 to 1. If  $h_3 = -1$  only left-handed helical structures are present in the fluid domain, whereas,  $h_3 = 1$  means the presence of only right-handed structures, hence,  $h_3 = 0$  denotes a reflectional symmetry of these structures. Descriptor  $h_4$  is the absolute value of  $h_3$  and its range is from 0 to 1, and it doesn't take into account the main direction of the rotation. The  $h_5$  consists in the ratio between the volume occupied by dominant direction  $V_d$  and the minor direction  $V_m$  of helical structures rotation.  $h_6$  is the ratio of the helicity intensity calculated respect volume  $V_d$  and  $V_m$ .

# Chapter 3

## Results

In this chapter, results of unsteady-state numerical simulations are visualized. Starting from Velocity distributions then, WSS-based descriptors and, moving on, helicity-based ones. Then dynamic pressure gradient and static pressure gradient for the same model with and without the stent are depicted, and, also, dynamic and static pressures for models' inlets and outlets. It should be noticed that the regions of interest are the stent and the aneurysm, for this reason all models were zoomed and sectioned there. The other vessels' zones, such as inlet and outlet, were cut-out in the figures.

# 3.1 Velocity Distribution

In this section Mean Velocity and Velocity calculated at peak systole (Peak Velocity) were considered. After stent deployment we aspect to find a reduction of flow in the aneurysmal sac and a lower velocity in the lumen, as the device attempts to isolate the aneurysm from the blood flow. Our expectations were fulfilled for models 2S and 3S but not for model 1S, which didn't show a relevant difference before the treatment, as shown in *Figure 3.1*. In fact, for this model a single stent is probably not sufficient.

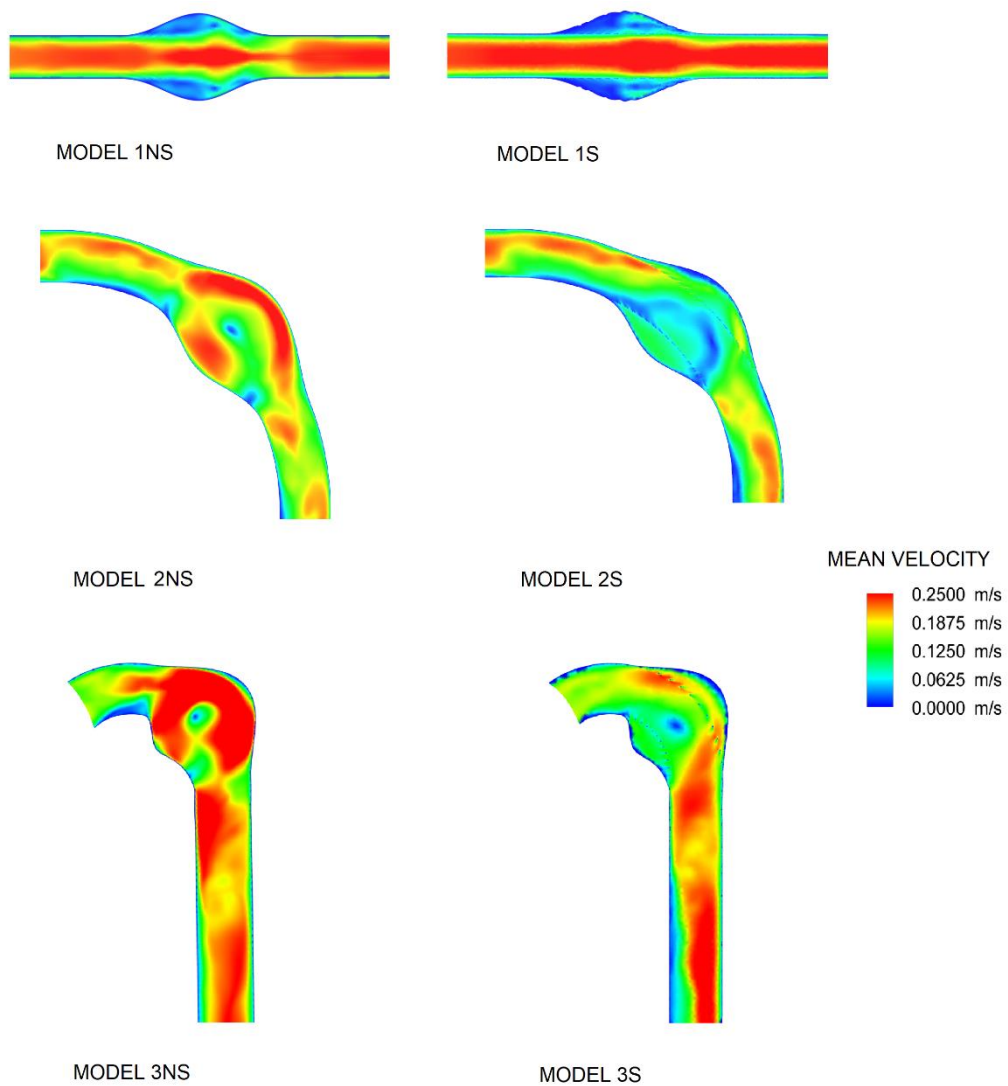


**Figure 3.1:** Mean Velocity distribution for all models

Instead, velocity at peak systole better shows the flow modulation into the lumen for all models, in *Figure 3.2* we can see that, after stent implantation, the velocity is re-sent to the center of the vessels.

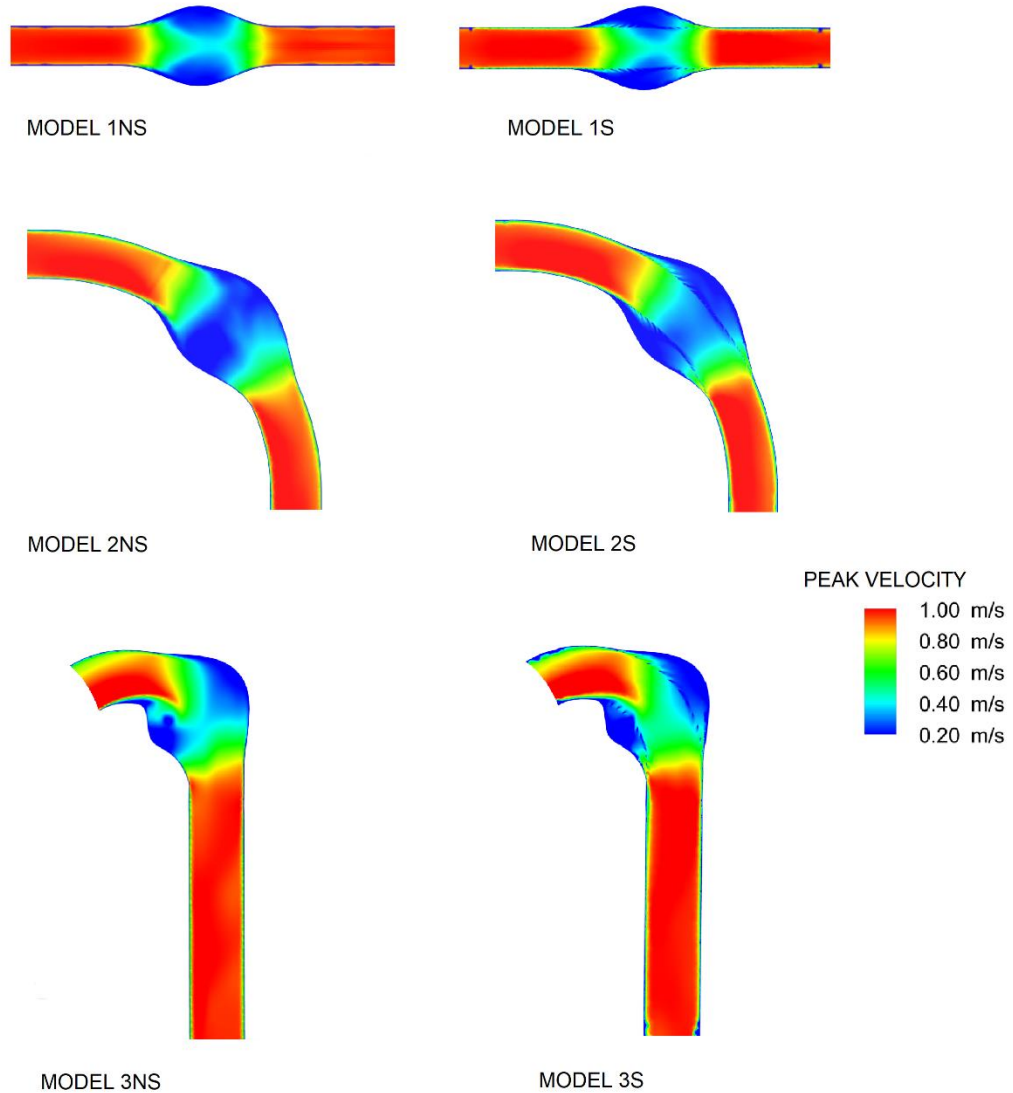


**Figure 3.2:** Peak Velocity distribution for all models.

## 3.2 WSS-Based Descriptors

Studies [36] [4] [6] have been demonstrated that bare-stent implantation stimulates the formation of ILT or other athero-protective structures. These structures shield the vessel's wall and, cooperating with the stent, isolate the aneurysm from the blood flow and reduce velocity in the aneurysmal sac. As velocity decrease we expect to find a lower value of TAWSS in the aneurysm and at the stent's cells, after stent implantation. As for model 2S and especially model 3S, TAWSS is supposed to be lower at the extrados of the aortic arch (*Figure 3.4*). In fact, during a cardiac cycle, this zone is subjected to higher velocity and higher pressure and is where most of aneurysms occur and tear. Fortunately, our expectations were right as we can see in *Figure 3.3*. In order to have a better representation of the interested descriptors values, low TAWSS for every model were cut-below at the threshold value of 20<sup>th</sup> (*Figure 3.5*) and 10<sup>th</sup> percentile and visualized isolated (*Figure 3.6*) 10<sup>th</sup> percentile was shown only in the extrados and intrados zones because it occurs only in these regions. For WSS-Based descriptors, the most noticeable differences before and after stent implantation appear in models 2S and 3S, in model 1NS and 1S, and this fact testifies the importance of vessel curvature and geometry, in straight tubular model stent benefits are less evident. All threshold percentile values of the WSS-Based descriptors, may be seen in *Table 2* and their percentage values are shown in *Table 3*.

Percentile Values	
TAWSS 20th [Pa]	0.725
TAWSS 10th [Pa]	0.5029
OSI 80th	0.2926
OSI 90th	0.3339
RRT 80th	2.9514
RRT 90th	4.6181

**Table 2.** Percentile values of WSS-Based descriptors

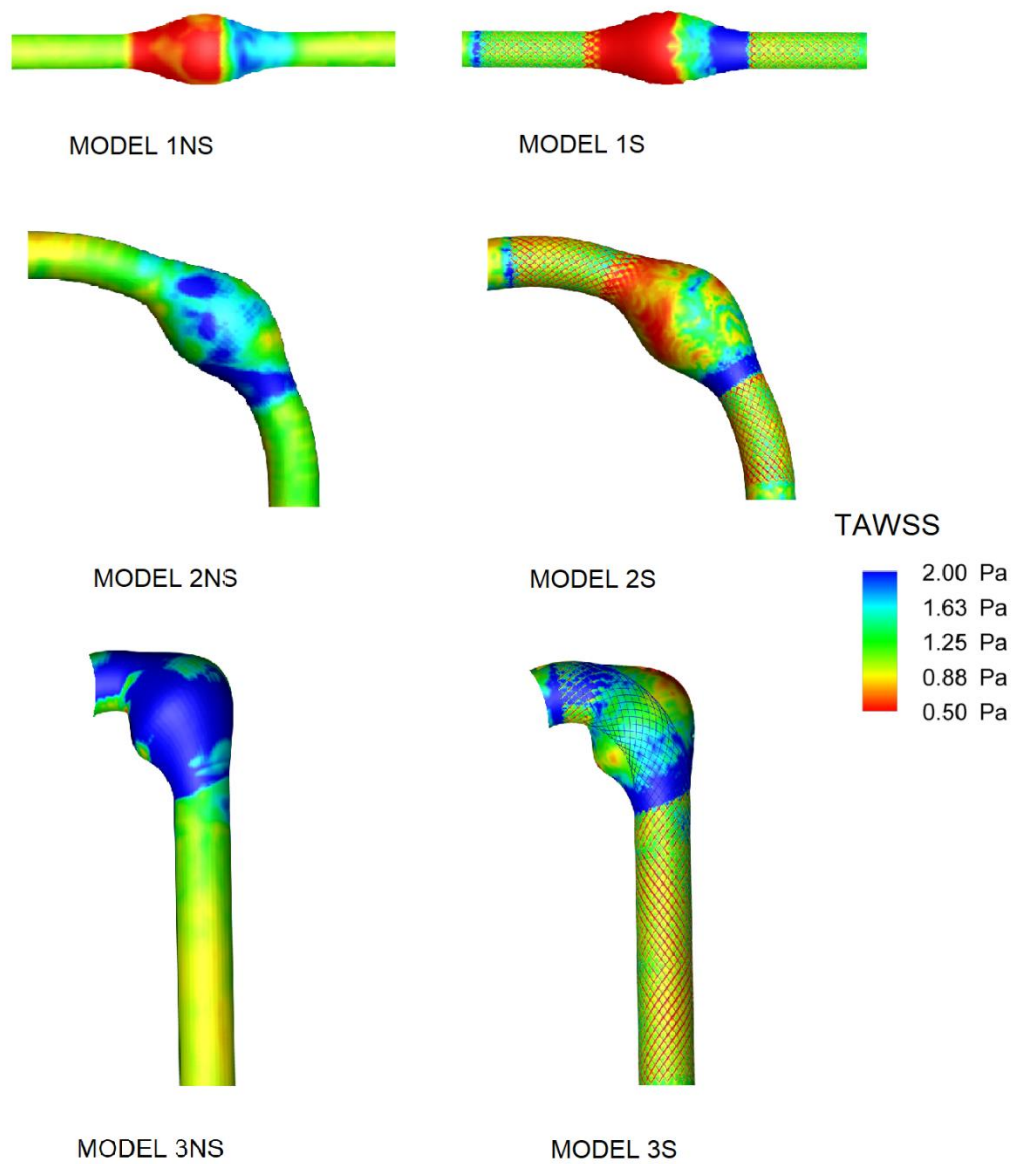


**Figure 3.3:** TAWSS distribution for every model in the frontal view

In the models 1NS and 1S TAWSS distribution is quite similar, the most noticeable difference, in the frontal view, is found between model 2NS and 2S at the inlet zone where stent benefits are remarkable as velocity decrease and so does the TAWSS descriptor, aneurysmal wall is no more stressed and the flow is now set in the lumen.

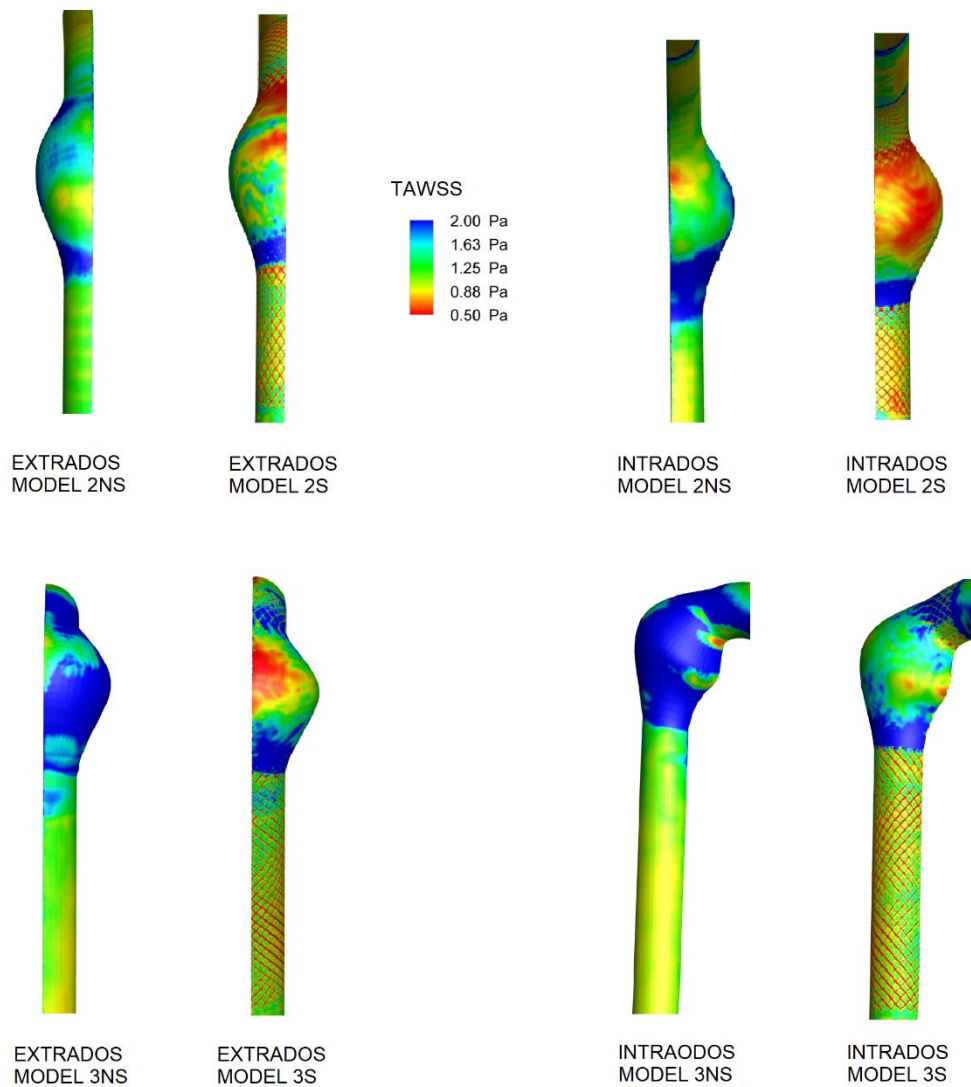


**Figure 3.4:** TAWSS distribution in the intrados and extrados zones for models 2NS 2S 3NS 3S

As we can see in the model 3S the extrados zone presents a very remarkable low TAWSS zone despite the model 3NS, and so does model 2S. This model, in particular, presents also a noticeable lower TAWSS than the 2NS in the intrados zone.

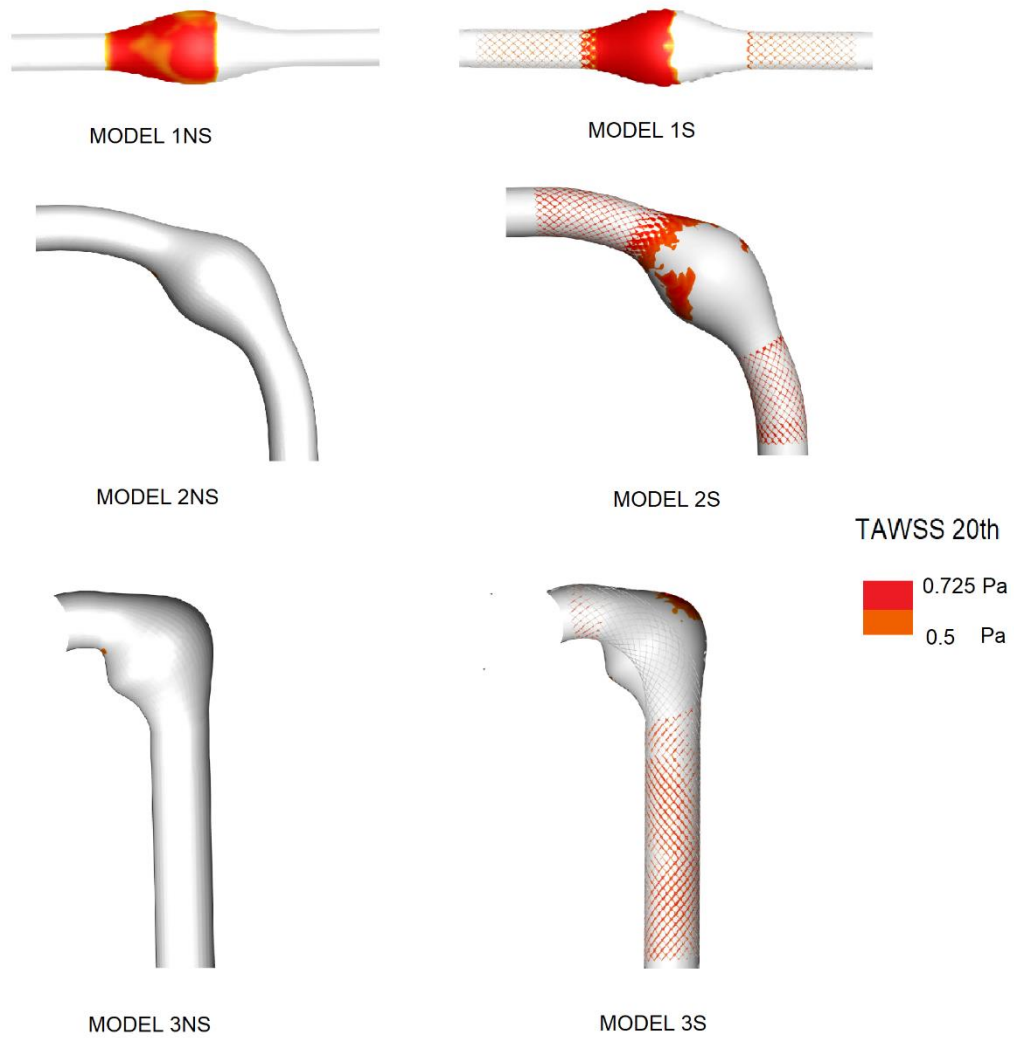


**Figure 3.5:** TAWSS 20<sup>th</sup> Percentile representation, frontal view

As said before, model 1NS and 1S don't present substantial differences in TAWSS distribution, although, lower values of TAWSS may be visualized in the stent cells for all stented models. The same conclusions of the previous figures may be drawn for models 2S and 3S.

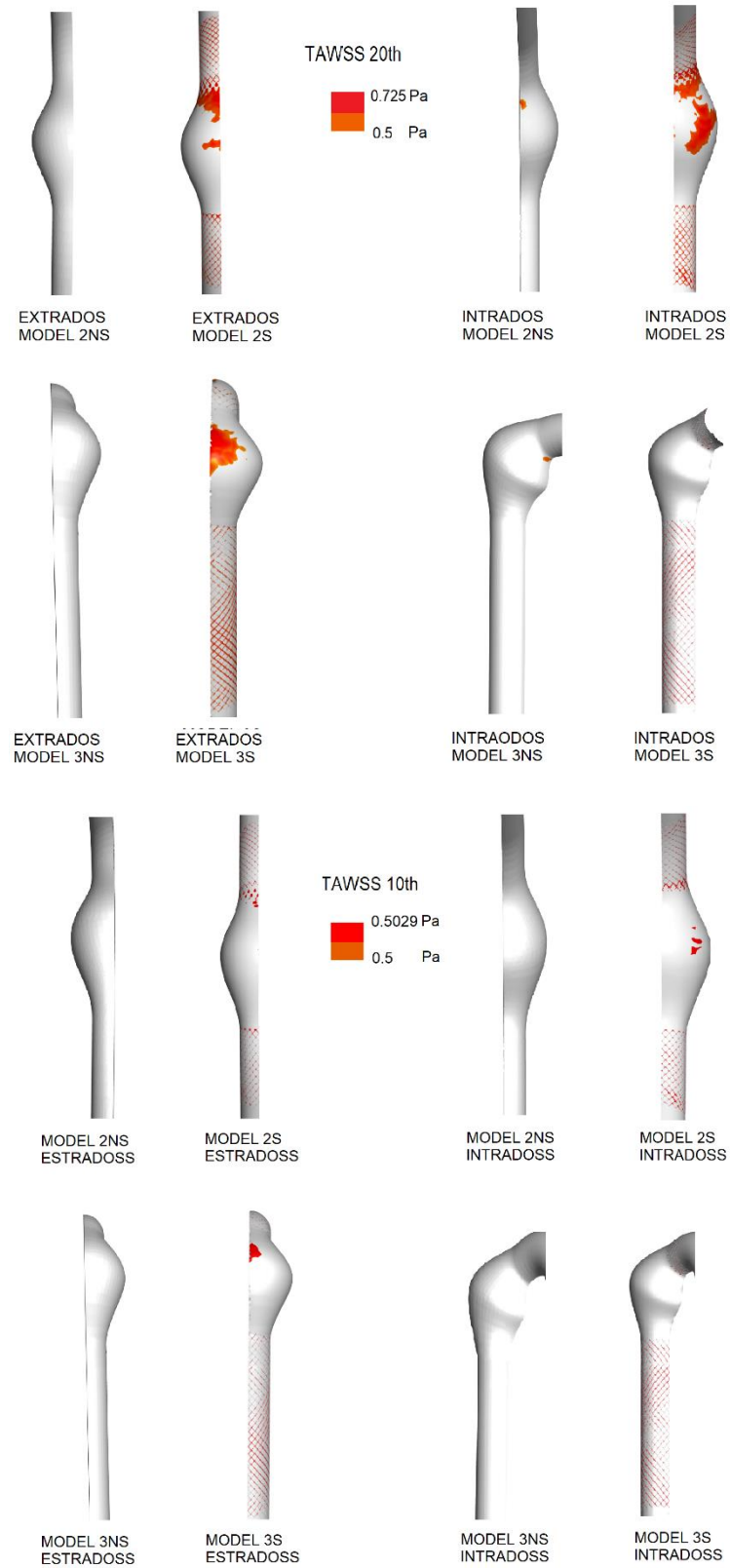


**Figure 3.6:** TAWSS 20<sup>th</sup> Percentile and 10<sup>th</sup> percentile representation in the extrados and intrados zones

OSI descriptor doesn't show substantial differences before and after stent implantation and high OSI occur in the same zones of the unstented and stented models *Figure 3.7*, in the intrados and extrados zone it slightly increases in the stented models *Figure 3.8*. In this case OSI 80<sup>th</sup> and 90<sup>th</sup> percentile values were calculated and visualized for every model as cut-above threshold value *Figure 3.10*

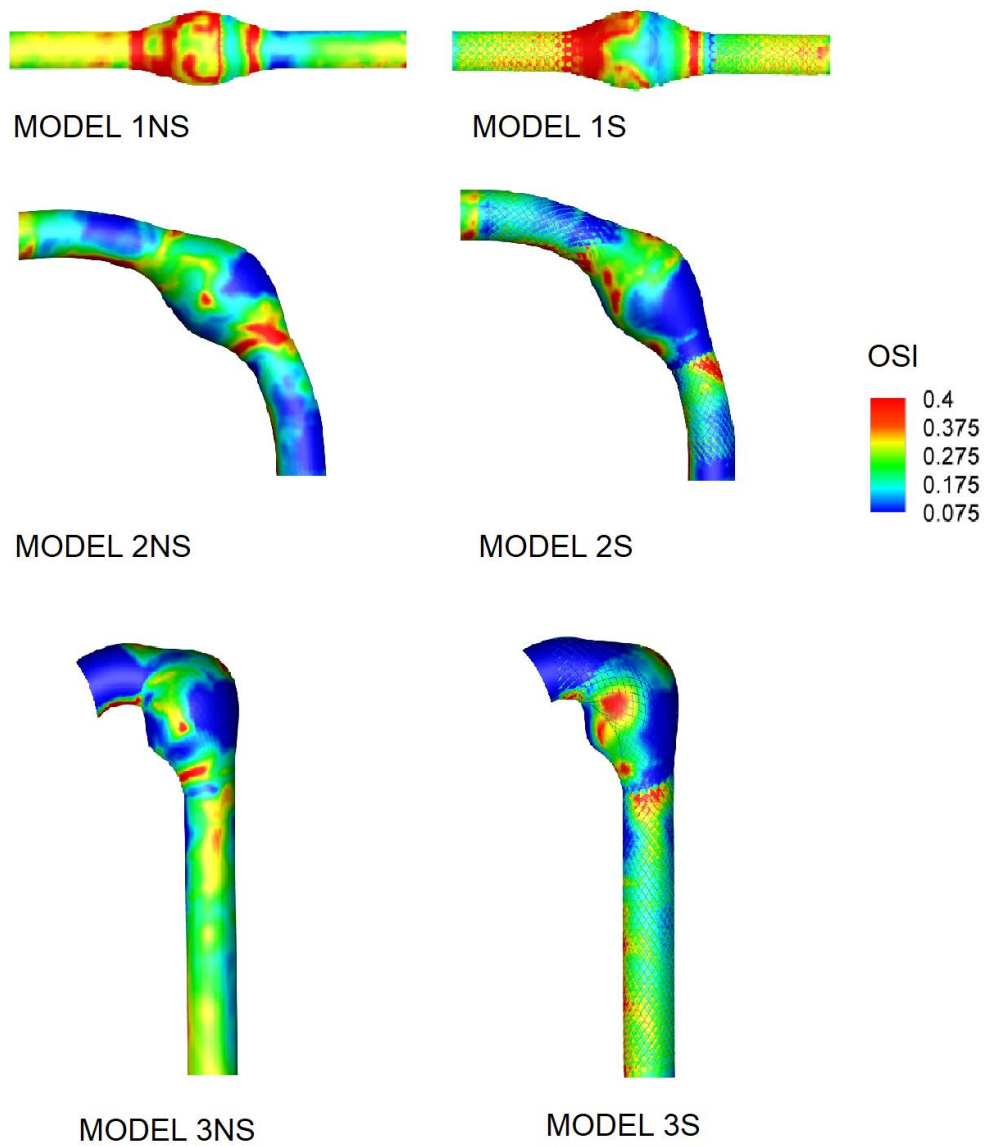


**Figure 3.7:** OSI distribution for every model in the frontal view

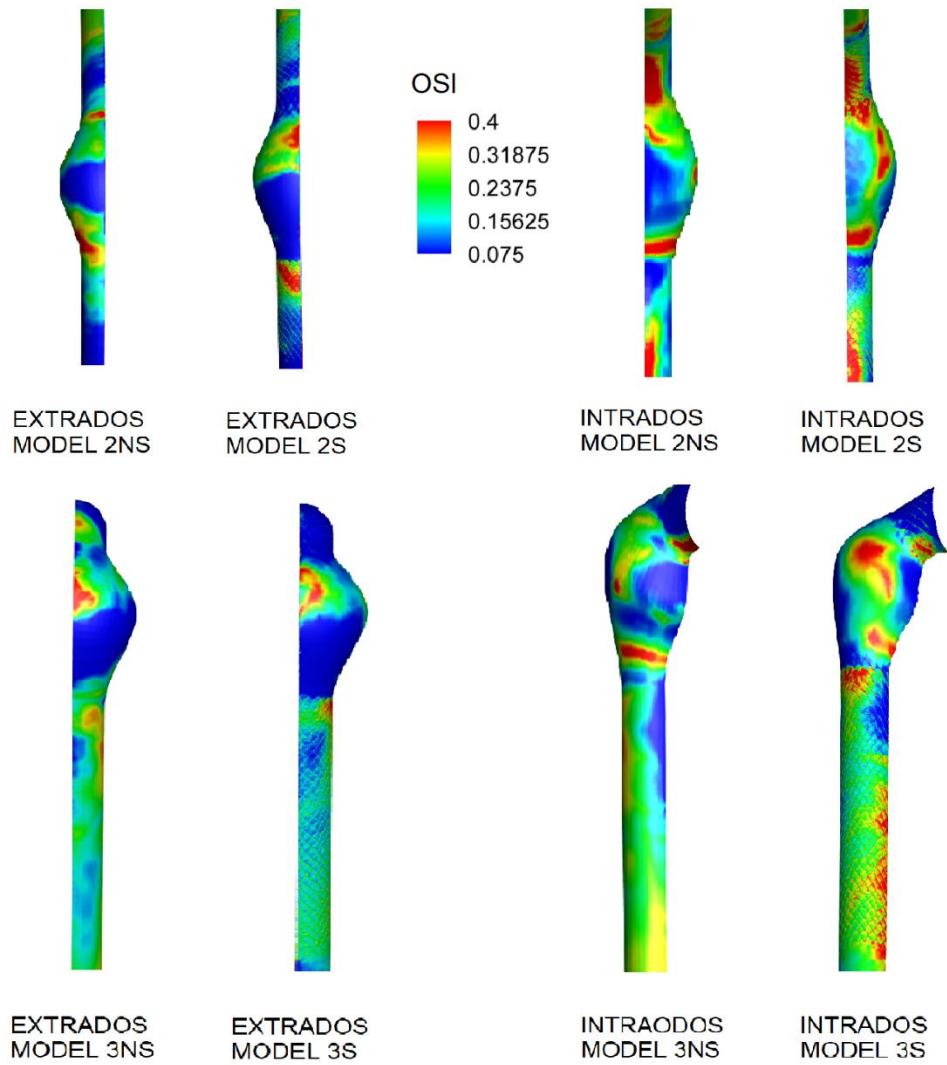


**Figure 3.8:** OSI distribution in the intrados and extrados zones for models 2NS 2S 3NS and 3S

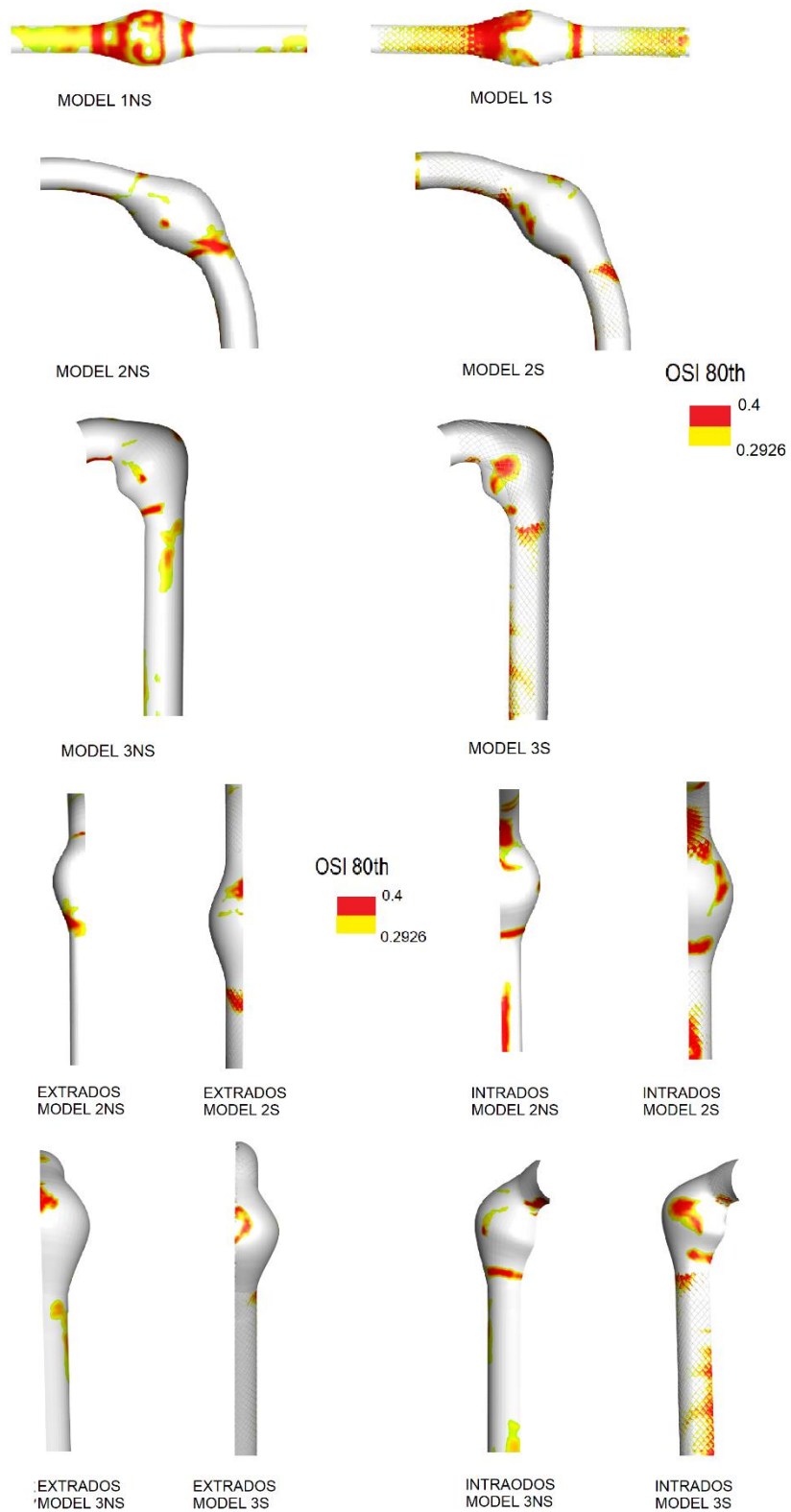


**Figure 3.9:** distribution of OSI 80<sup>th</sup> percentile for all models in their frontal views and in the intrados and extrados zone of models 2NS 2S 3NS and 3S

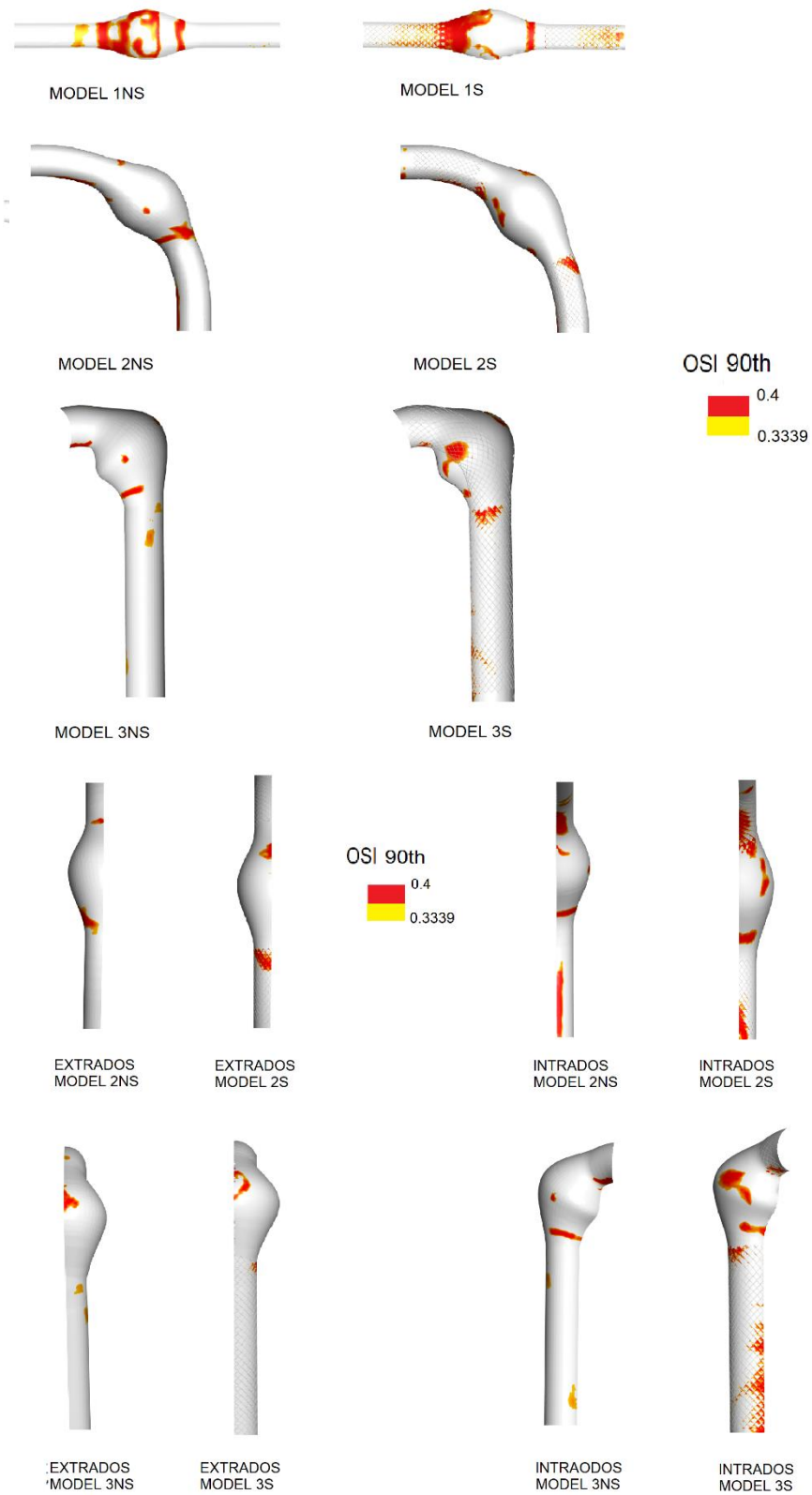


**Figure 3.10:** distribution of OSI 90<sup>th</sup> percentile for all models in their frontal views and in the intrados and extrados zone of models 2NS 2S 3NS and 3S

RRT is supposed to be higher in the stented models, due to particles deposition and athero-protective structures formation, as we can see in *Figure 3.11*. Relative Residence Time is higher in stented models also because TAWSS is lower and OSI is higher and this descriptor is a combination of the other two as seen in formula (2.9).

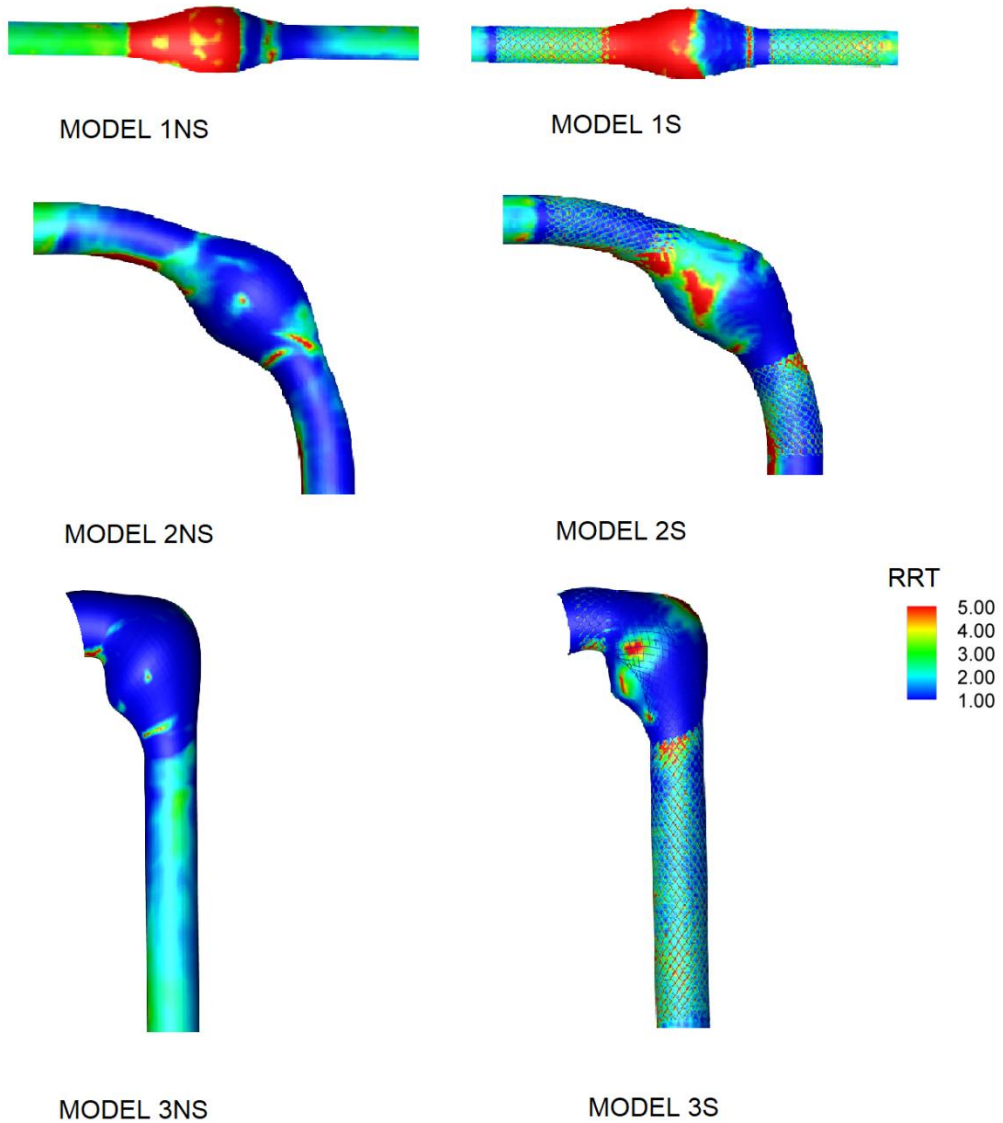


**Figure 3.11:** RRT distribution for all models, frontal view

From model 1NS and 1S the differences aren't so evident, the high RRT values seems to stay concentrated in the inlet zone of the aneurysm's sac. In the other two model new high zones occur in the aneurysm wall, and in the same zones characterized by low TAWSS and high OSI. Other differences might be noticed in the intrados and extrados zones *Figure 3.12*.

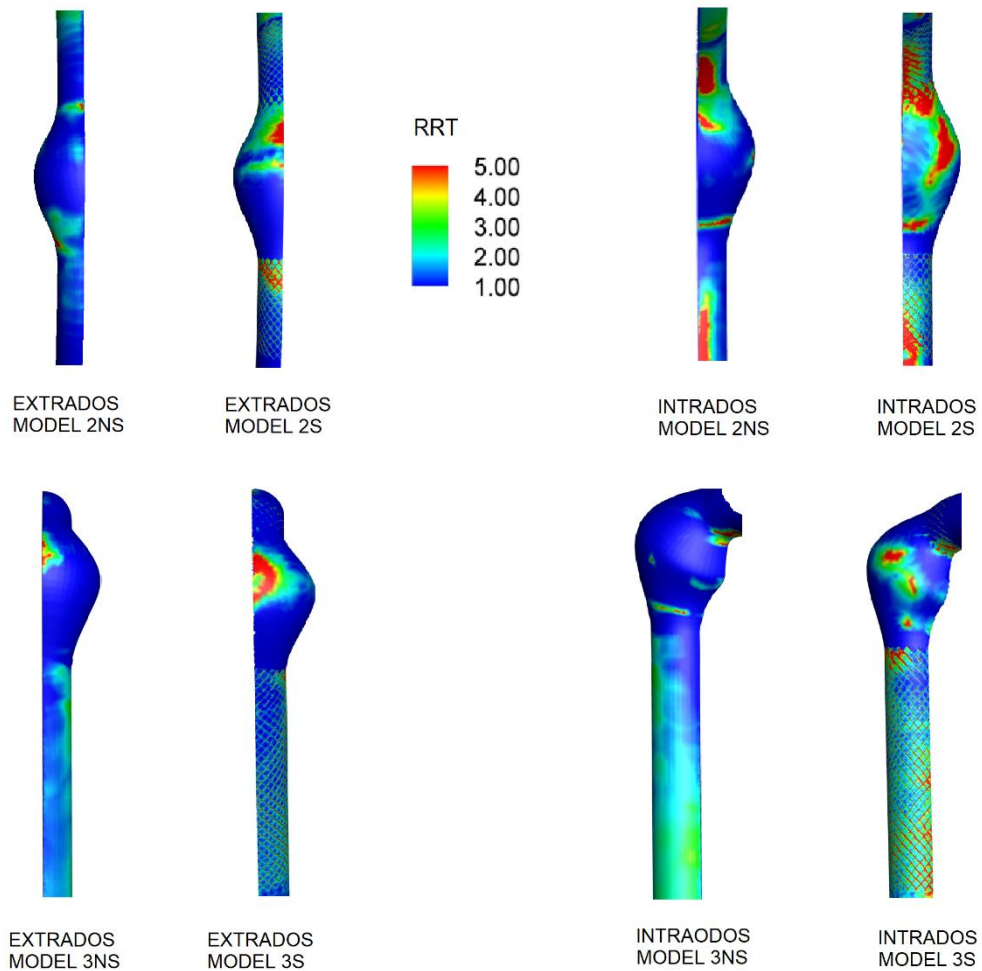


**Figure 3.12:** RRT distribution in the extrados and intrados zones of model 2NS 2S 3NS and 3S

In model 2S differences from 2NS are noticeable in both intrados and extrados, while, for model 3S are more evident in the extrados, in particular, in the zone with low TAWSS where aneurysm usually tears. As for OSI, RRT 80<sup>th</sup> and 90<sup>th</sup> percentile values were calculated and visualized for every model as cut-above threshold value *Figure 3.13 and Figure 3.14*.

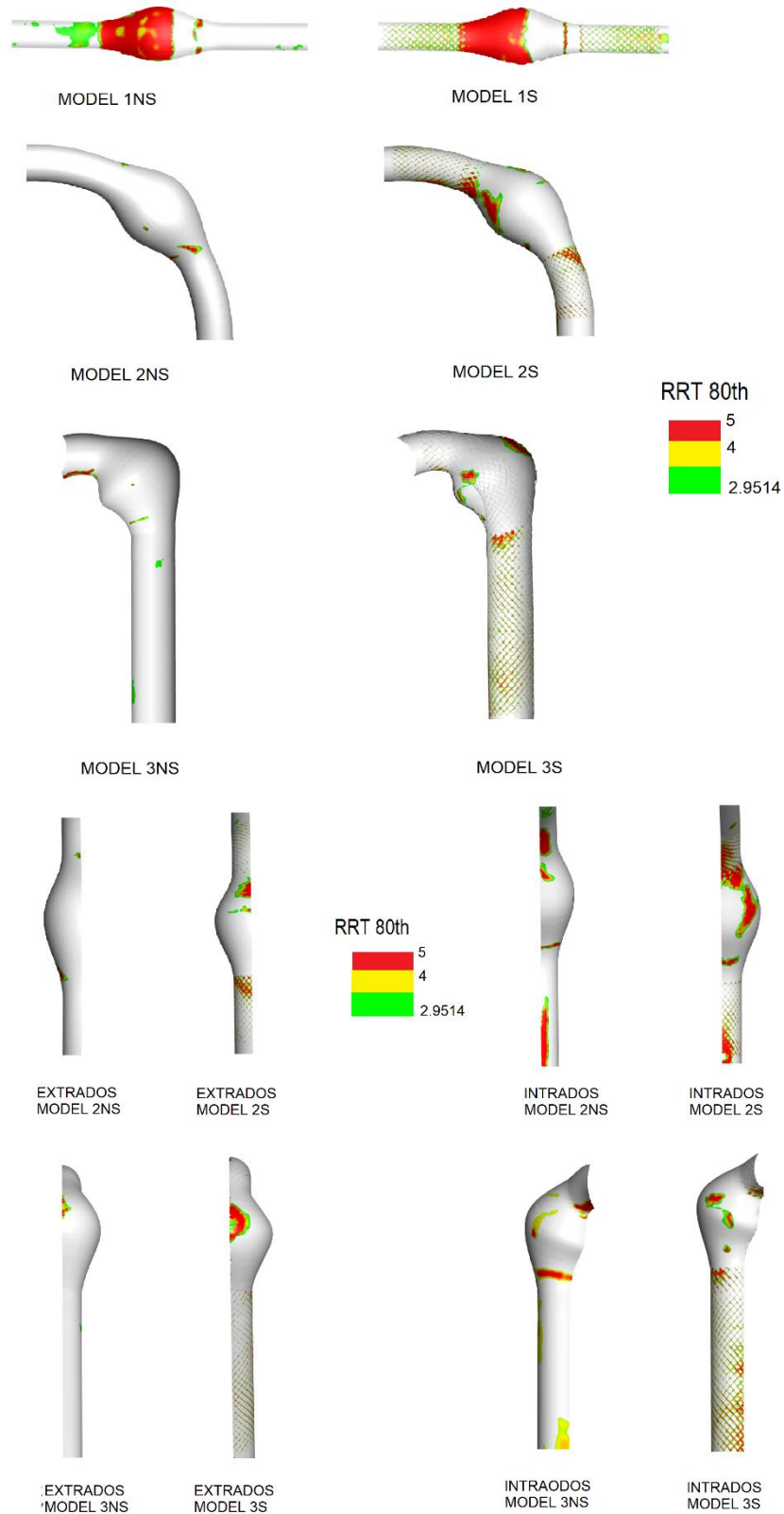


**Figure 3.13:** distribution of RRT 80<sup>th</sup> percentile for all models in their frontal views and in the intrados and extrados zone of models 2NS 2S 3NS and 3S

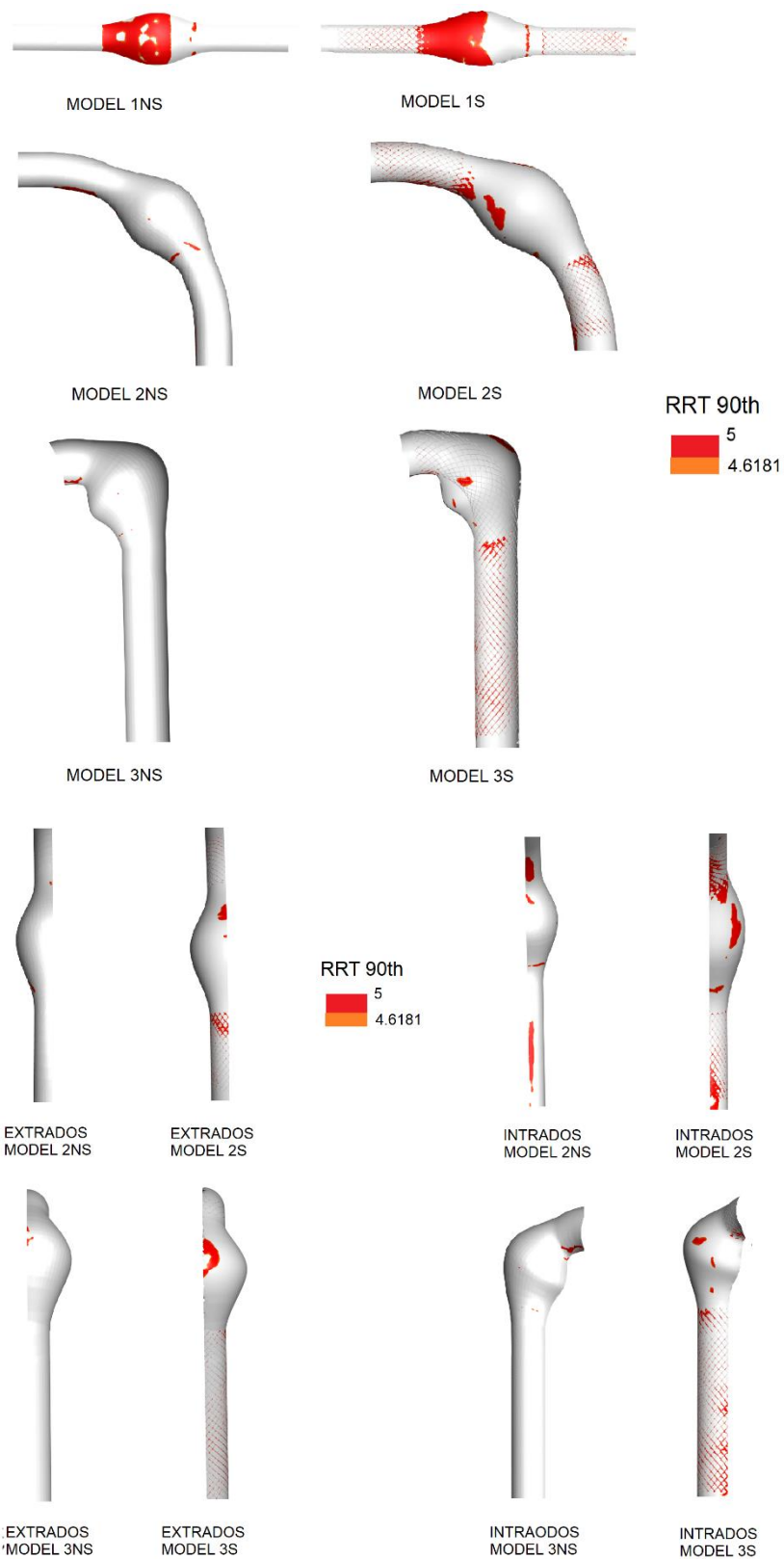


**Figure 3.14:** distribution of RRT 90<sup>th</sup> percentile for all models in their frontal views and in the intrados and extrados zone of models 2NS 2S 3NS and 3S

	<b>MODEL 1NS</b>	<b>MODEL 1S</b>	<b>MODEL 2NS</b>	<b>MODEL 2S</b>	<b>MODEL 3NS</b>	<b>MODEL 3S</b>
<b>TAWSS 20th</b>	18.48 %	18.68 %	0.13 %	11.18 %	0.95 %	8.96 %
<b>TAWSS 10th</b>	9.21 %	14.56 %	0 %	2.81 %	0 %	3.24 %
<b>OSI 80th</b>	44.74 %	41.59 %	17.28 %	15.29 %	27.57 %	12.93 %
<b>OSI 90th</b>	22.4 %	24.3 %	7.91 %	9.53 %	6.1 %	6.44 %
<b>RRT 80th</b>	32.28 %	31.1 %	7.1 %	13.37 %	5.49 %	10.1 %
<b>RRT 90th</b>	17.24 %	16.7 %	2.59 %	5.7 %	1.41 %	4.58 %

**Table 3.** Percentage values of WSS-Based descriptors percentiles

### 3.3 Helicity-Based Descriptors

To visualize counter-rotating structures in the bulk flow LNH descriptor have been utilized. It has been considered at mean velocity, LNH Mean, and at peak systole, LNH Peak. For the first descriptor, shown in *Figure 3.15*, the chosen threshold values were  $\pm 0.2$ , and for the second, shown in *Figure 3.16*, the values were  $\pm 0.4$ . The blue-colored zones indicate structures with a clockwise rotation, whereas, the red-colored, the ones with a counter-clockwise rotation. LNH didn't show an effective decrease of these structures.

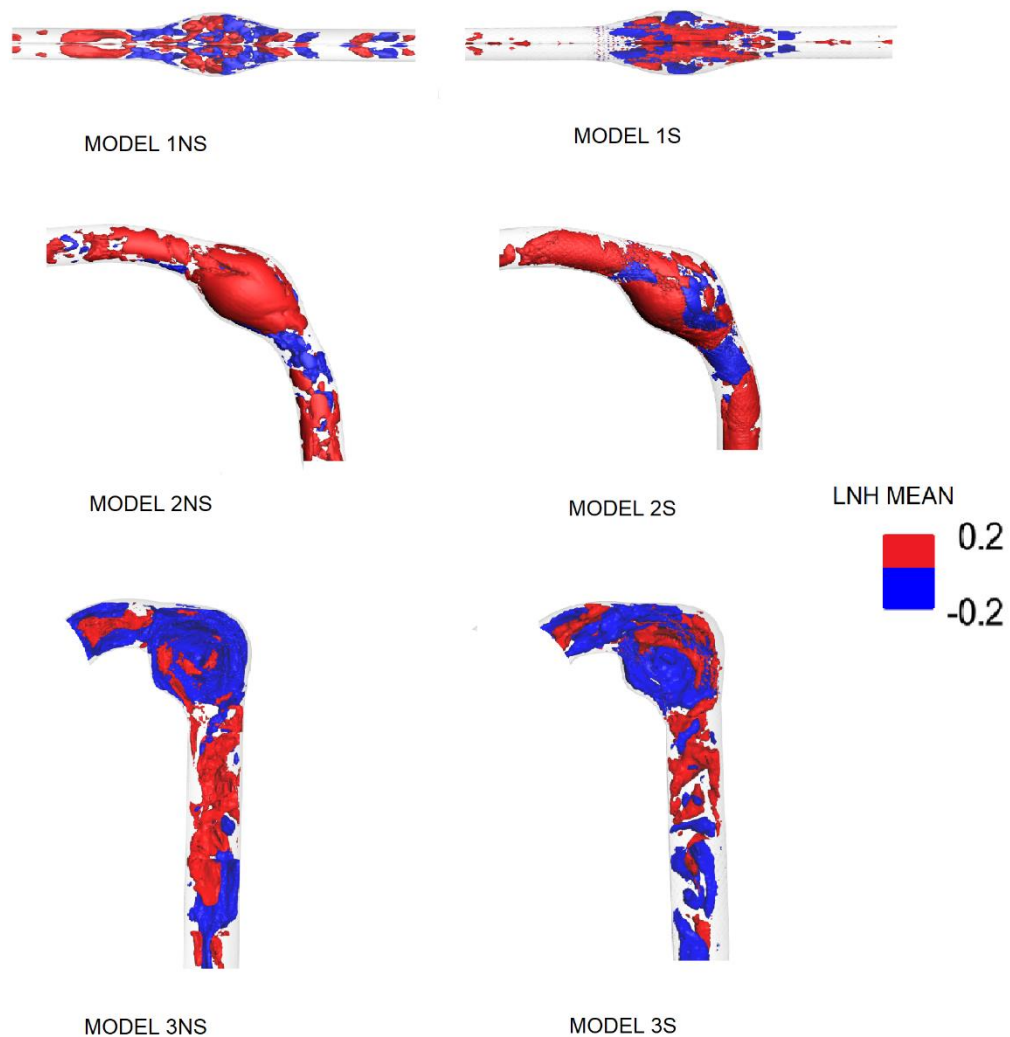


**Figure 3.15:** LNH Mean distribution for all models in the frontal view

for the LNH Peak descriptor, shown in *Figure 3.16*, the values considered were  $\pm 0.4$ . It demonstrates more efficaciously the stent influence, in fact we can see a noticeable reduction of the structures in stented models, and they are mostly located in the lumen vessels.

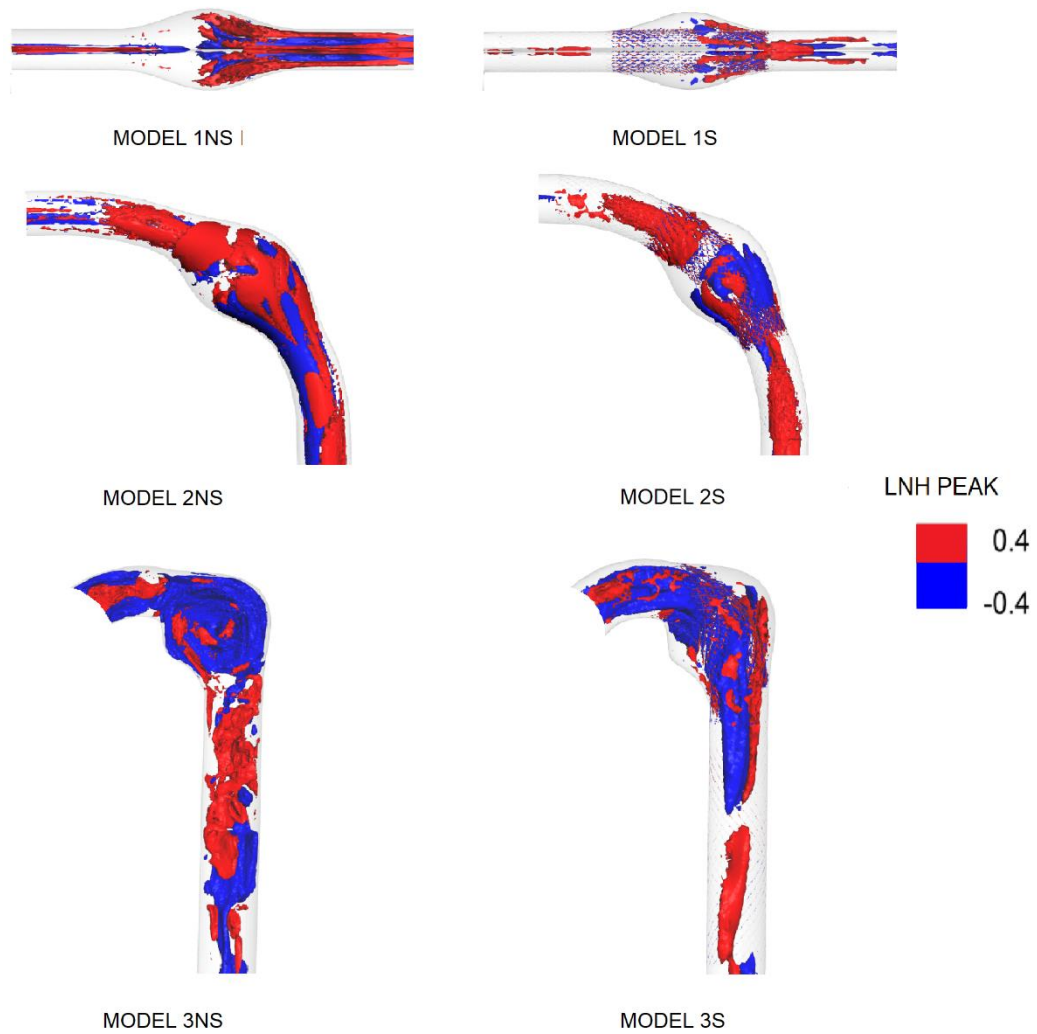


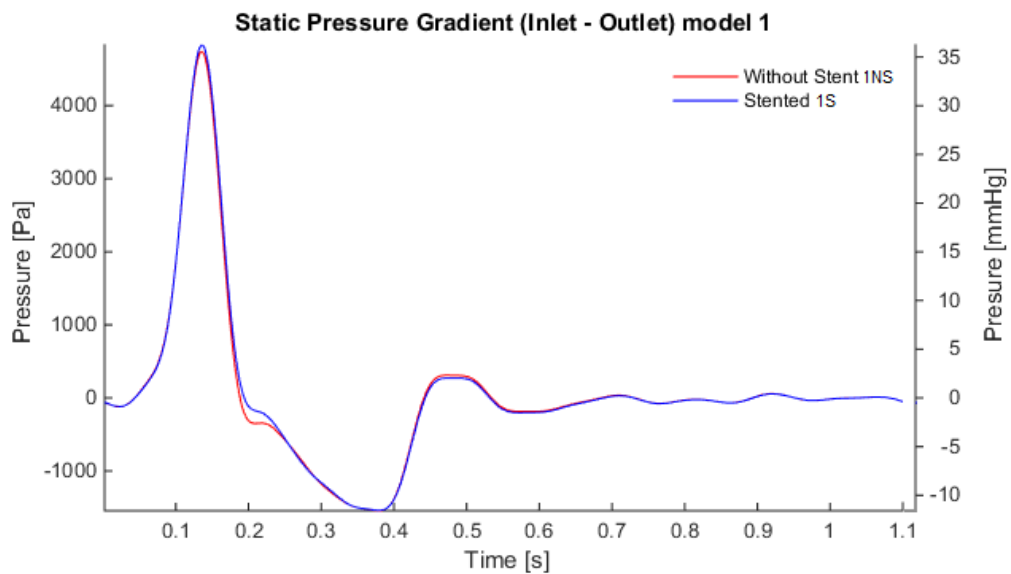
**Figure 3.16:** LNH Peak representation for all models in the frontal view

	<b>h1</b>	<b>h2</b>	<b>h3</b>	<b>h4</b>	<b>h5</b>	<b>h6</b>
<b>MODEL 1NS</b>	0.18	0.96	0.19	0.19	1.44	2.08
<b>MODEL 1S</b>	0.08	0.83	0.096	0.096	1.59	1.36
<b>MODEL 2NS</b>	2.89	5.06	0.57	0.57	2.34	10.06
<b>MODEL 2S</b>	1.52	2.91	0.52	0.52	2.56	5.94
<b>MODEL 3NS</b>	-3.47	6.48	-0.54	0.54	1.94	8.41
<b>MODEL 3S</b>	-1.98	3.88	-0.51	0.51	2.53	5.64

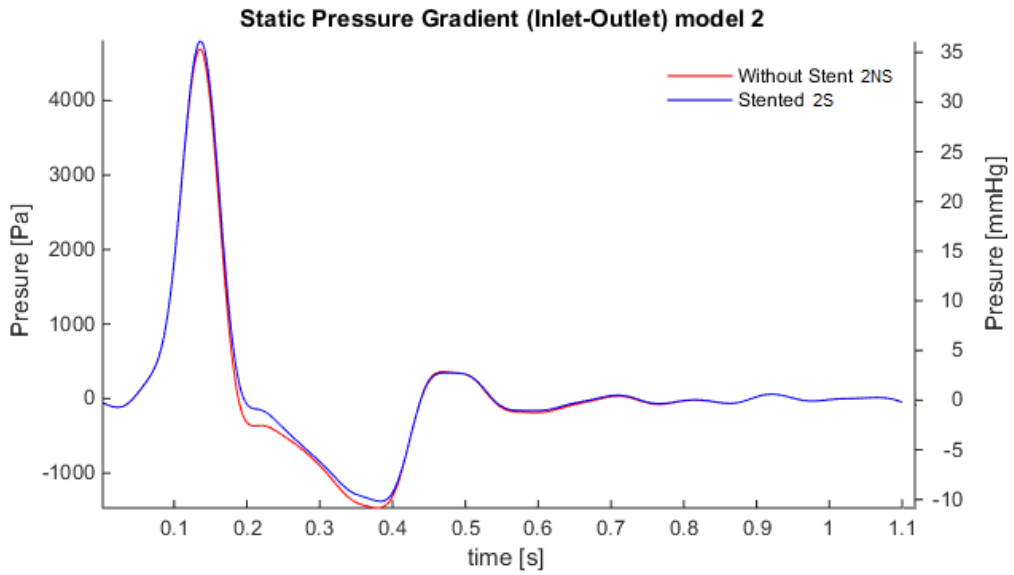
**Table 4:** Quantitative Helicity Indexes for all models

## 3.4 Pressure Distribution

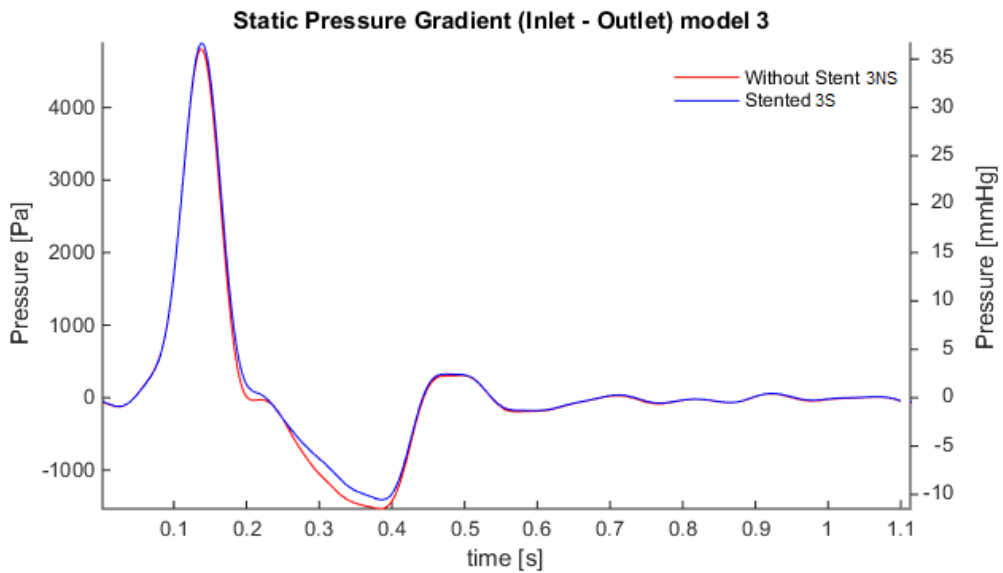
In this section Dynamic and Static Pressure Gradients are described, then the single models' inlet and outlet pressures. After the device deployment static pressure gradient, as seen in *Figure 3.17* 3.17 3.19, didn't vary significantly, instead, dynamic pressure gradient showed a remarkable improvement of pressure in stented models, since a minor amount of pressure is focused at the aneurysmal wall, and that is another consequence of velocity reduction, as we can see in *Figures 3.20* 3.21 3.22. Pressure gradients were calculated from inlet surface to outlet surface, in both [Pa] and [mmHg], to better visualize the variations; the two scales follow the relationship: 1 mmHg = 133.322 Pa.



**Figure 3.17:** Static Pressure Gradient for models 1NS and 1S

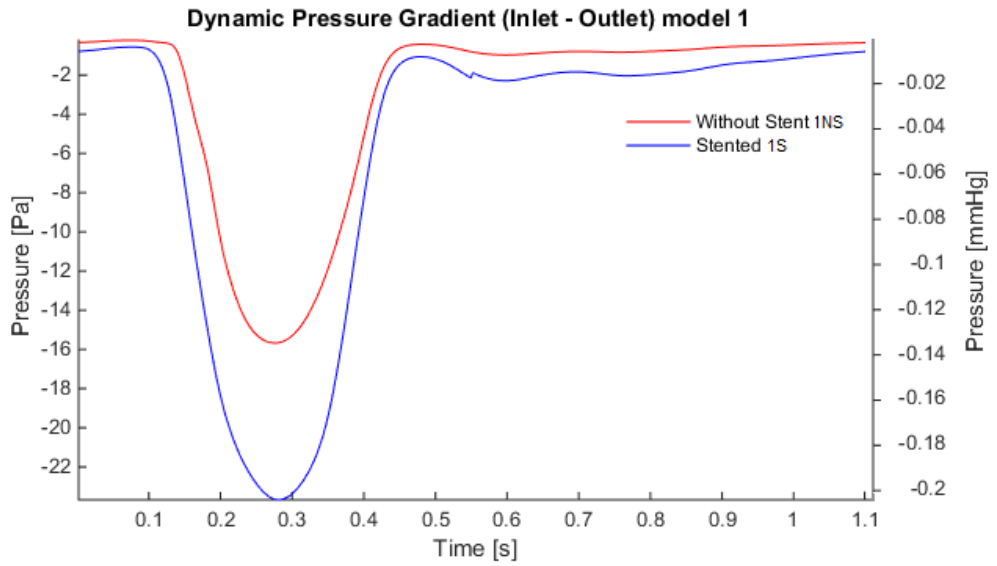


**Figure 3.18:** Static Pressure Gradient for models 2NS and 2S

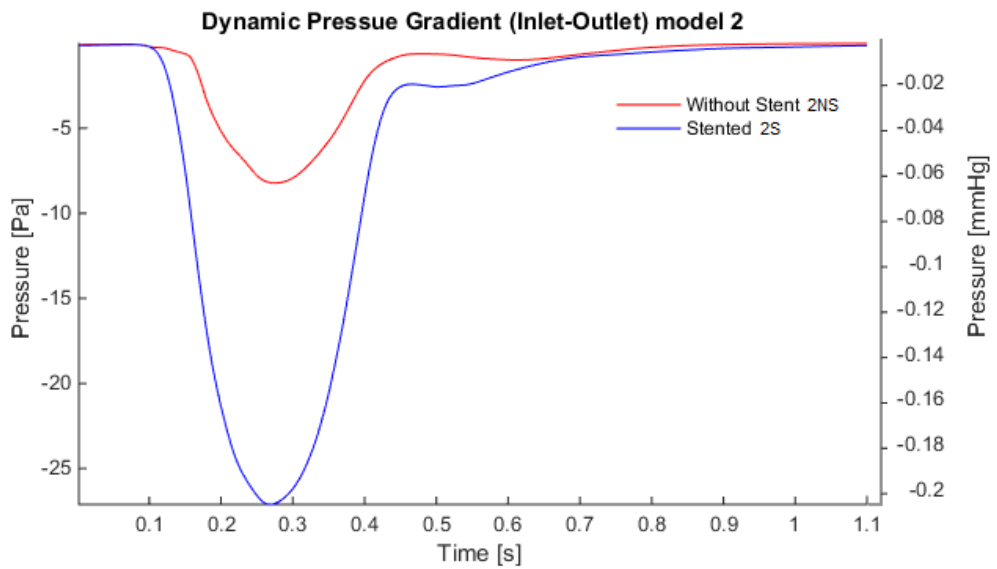


**Figure 3.19:** Static Pressure Gradient for models 3NS and 3S

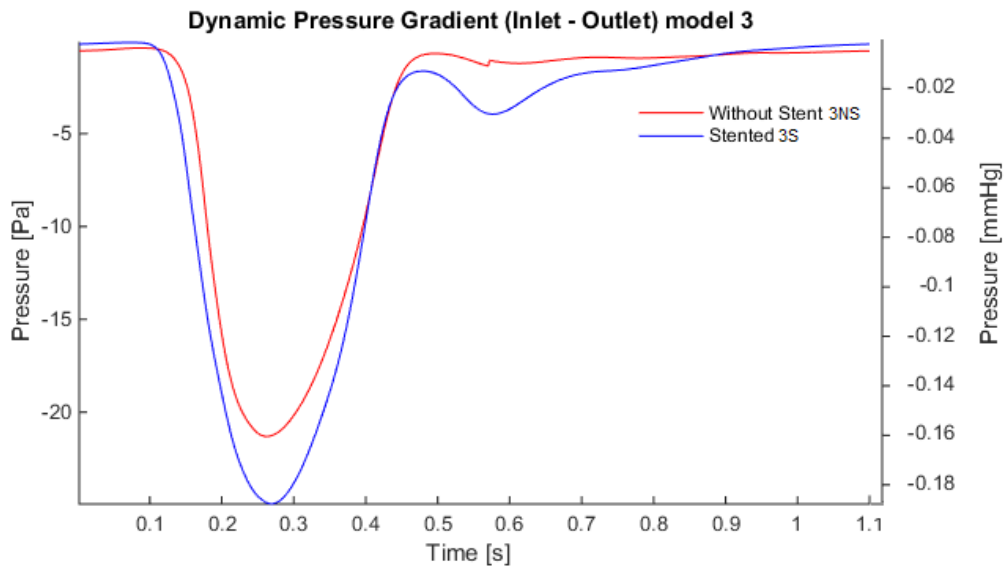
In both scales the differences from unstented and stented models are barely evident. They present a similar curve trend of the inlet-flow curve shown in *Figure 2.5*. Below are reported the dynamic gradients.



**Figure 3.20:** Dynamic Pressure Gradient for models 1NS and 1S



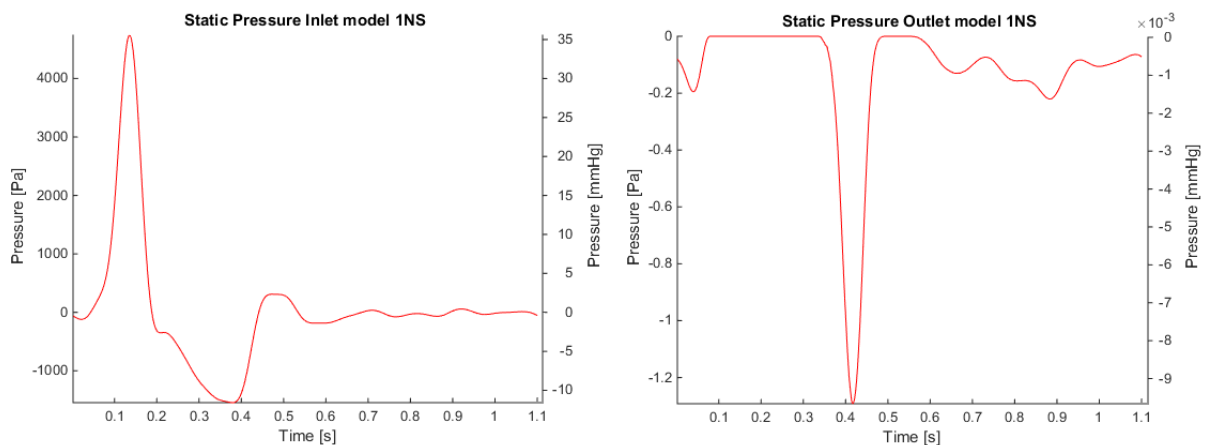
**Figure 3.21:** Dynamic Pressure Gradient for models 2NS and 2S

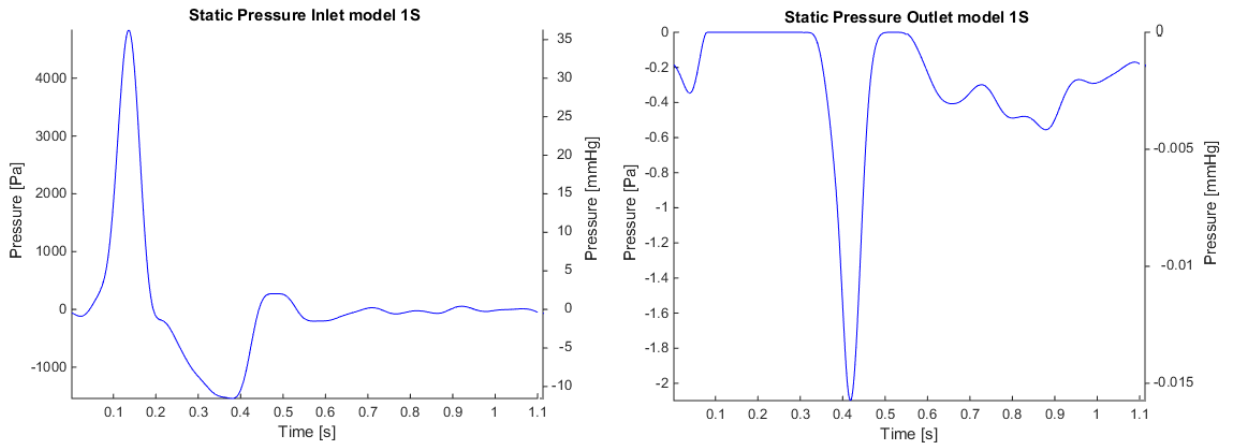


**Figure 3.22:** Dynamic Pressure Gradient for models 3NS and 3S

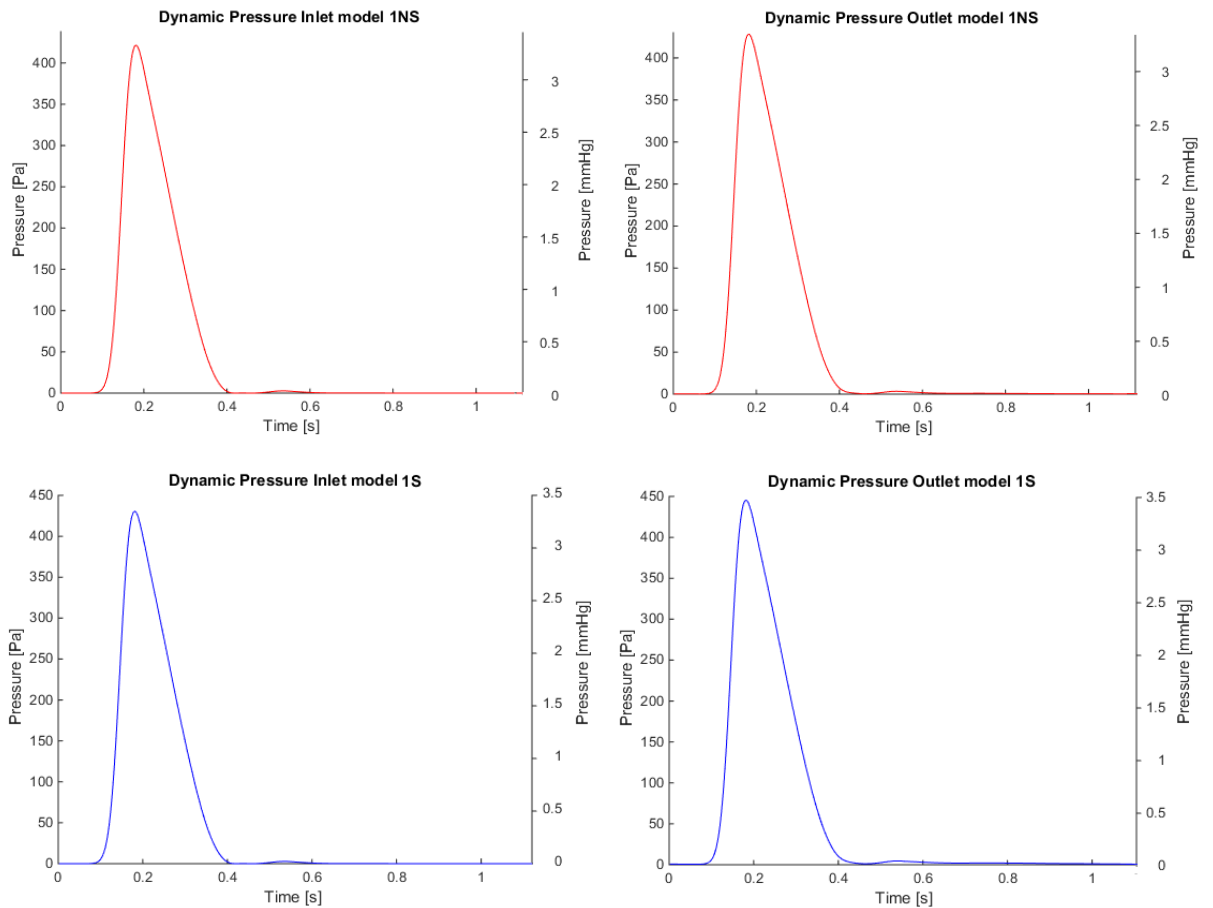
The maximum difference of dynamic pressure gradient between unstented and stented models occur at peak systole, in figures above represented as the negative maximum peak. For models 1NS and 1S the difference is near 9 Pa or 0.0675 mmHg, for models 2NS and 2S the difference is the most remarkable, almost 20 Pa, equal to 0.15 mmHg. Finally, models 3NS and 3S show the minimum difference which is equal to almost 4 Pa or 0.03 mmHg.

We also measured the singles static and dynamic pressures at the inlets and outlets of the single models, reclaiming the previous notations, unstented models' curve are red-colored, while, stented ones are blue-colored. We neared the inlet and outlet pressure for every model to better show that at the outlet the pressure was quite higher.



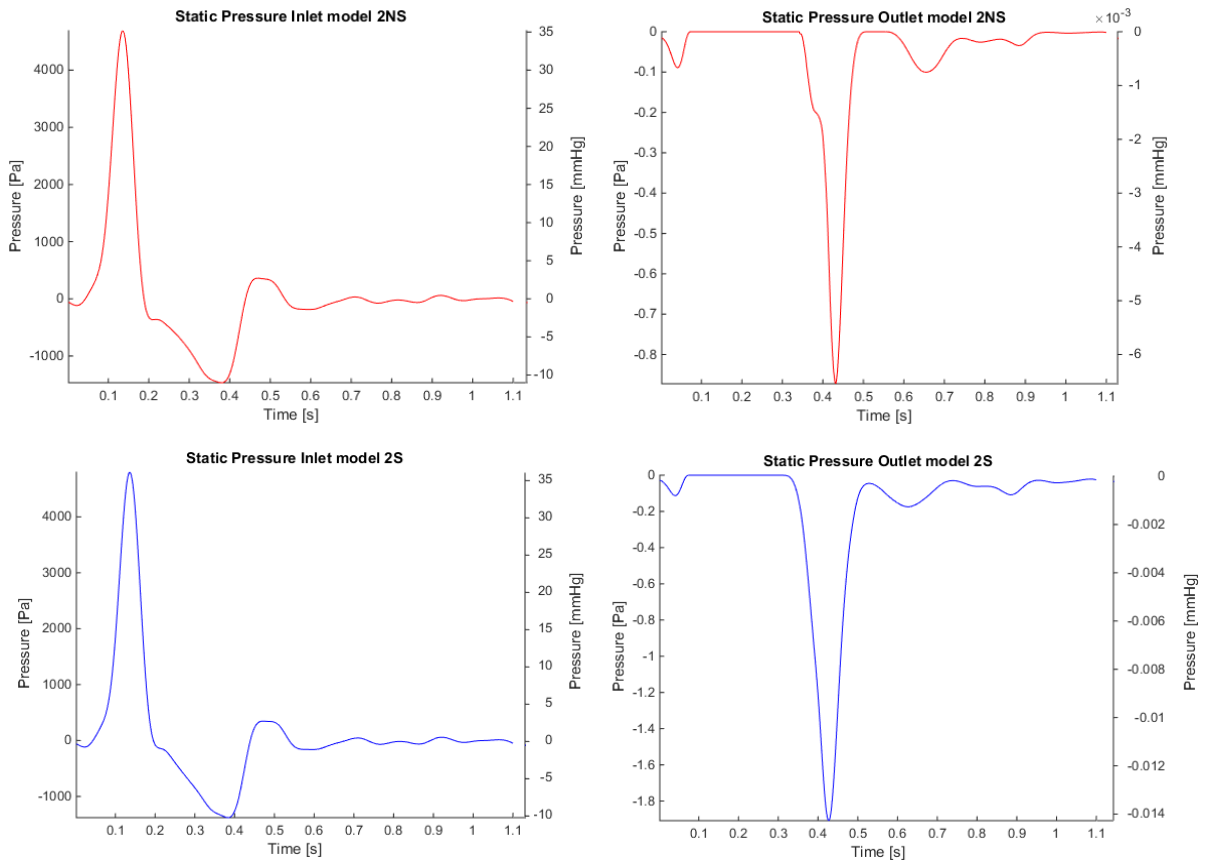


**Figure 3.23:** Static pressure at inlet and outlet surface for model 1NS (red) and for 1S (blue)

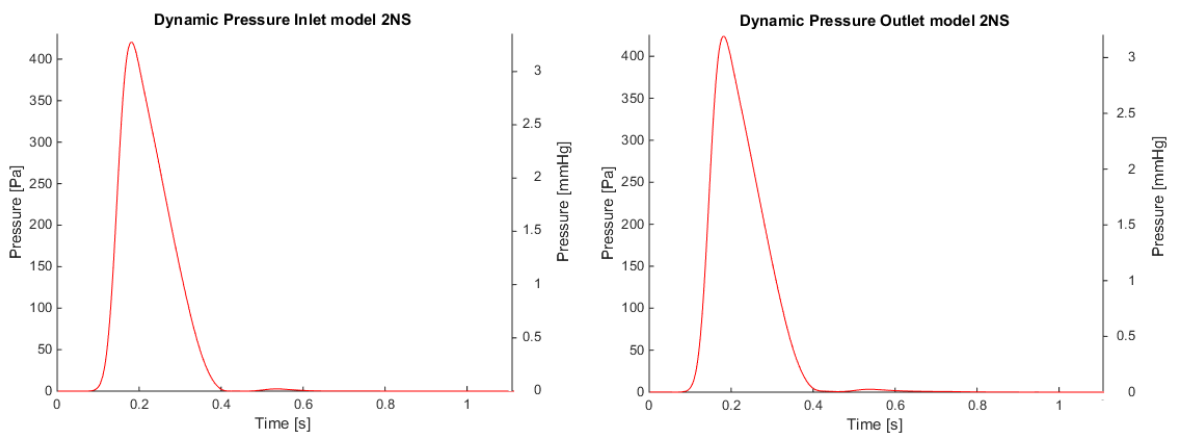


**Figure 3.24:** Dynamic pressure at inlet and outlet surface for model 1NS (red) and for 1S (blue)

it should be noticed that for dynamic pressure of stented models the scale maximum was higher, set at 450 Pa or 3.5 mmHg, respect to the unstented models, in which was 400 Pa or 3 mmHg.



**Figure 3.25:** Static pressure at inlet and outlet surface for model 2NS (red) and for 2S (blue)



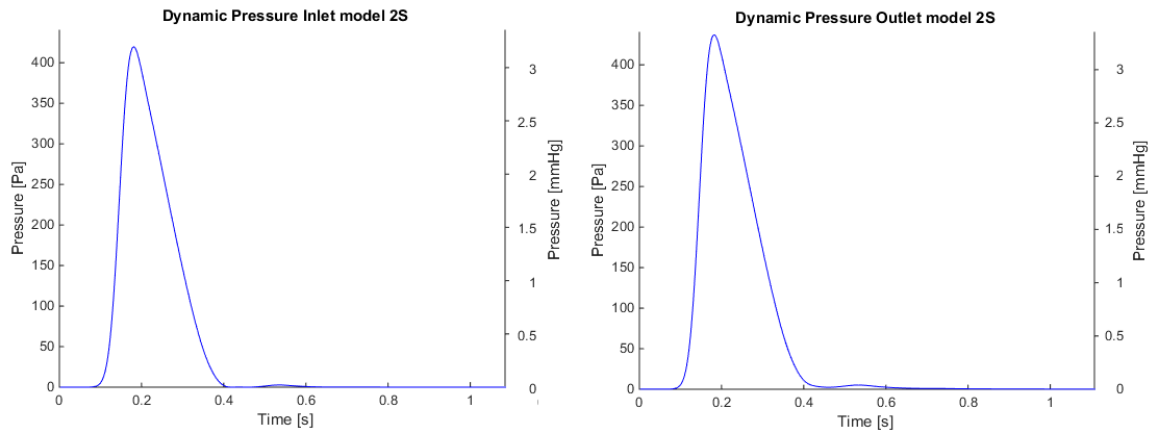


**Figure 3.26:** Dynamic pressure at inlet and outlet surface for model 2NS (red) and for 2S (blue)

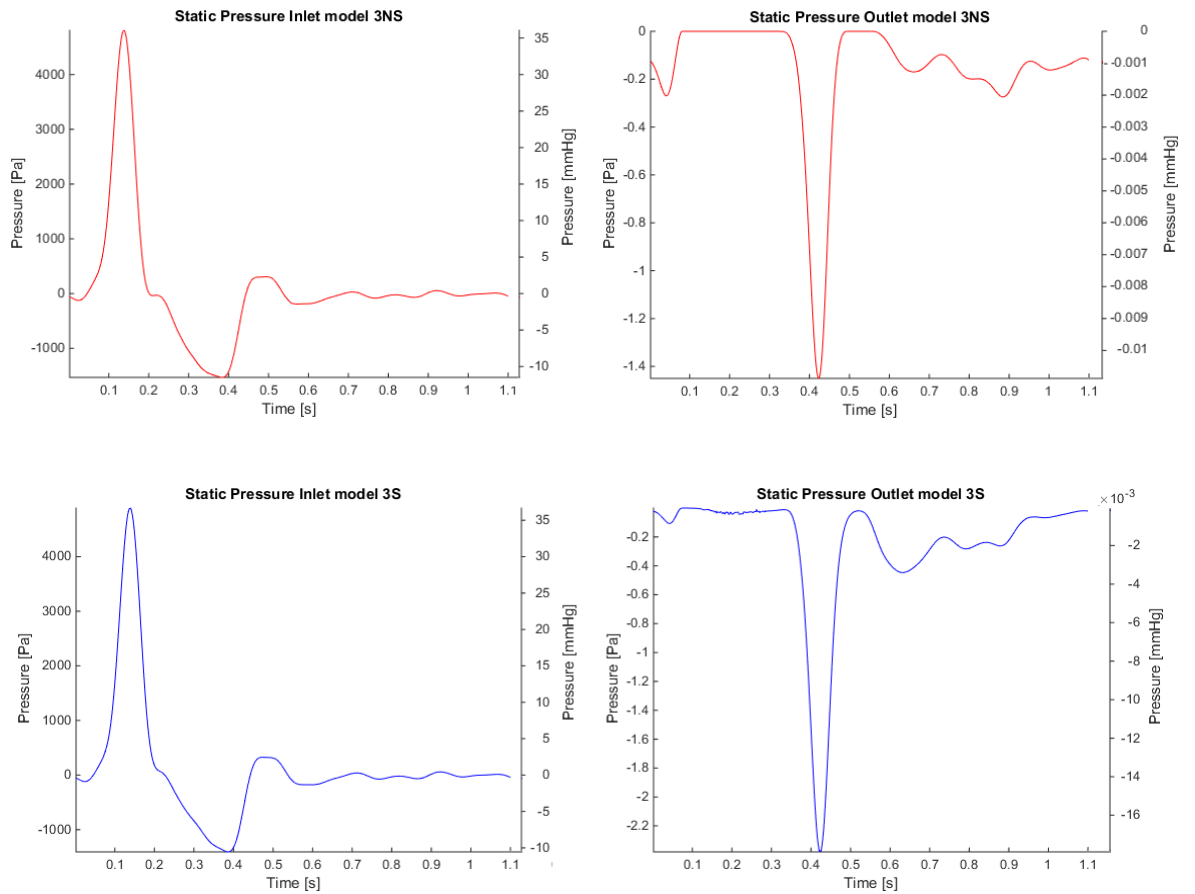


**Figure 3.27:** Static pressure at inlet and outlet surface for model 3NS (red) and for 3S (blue)

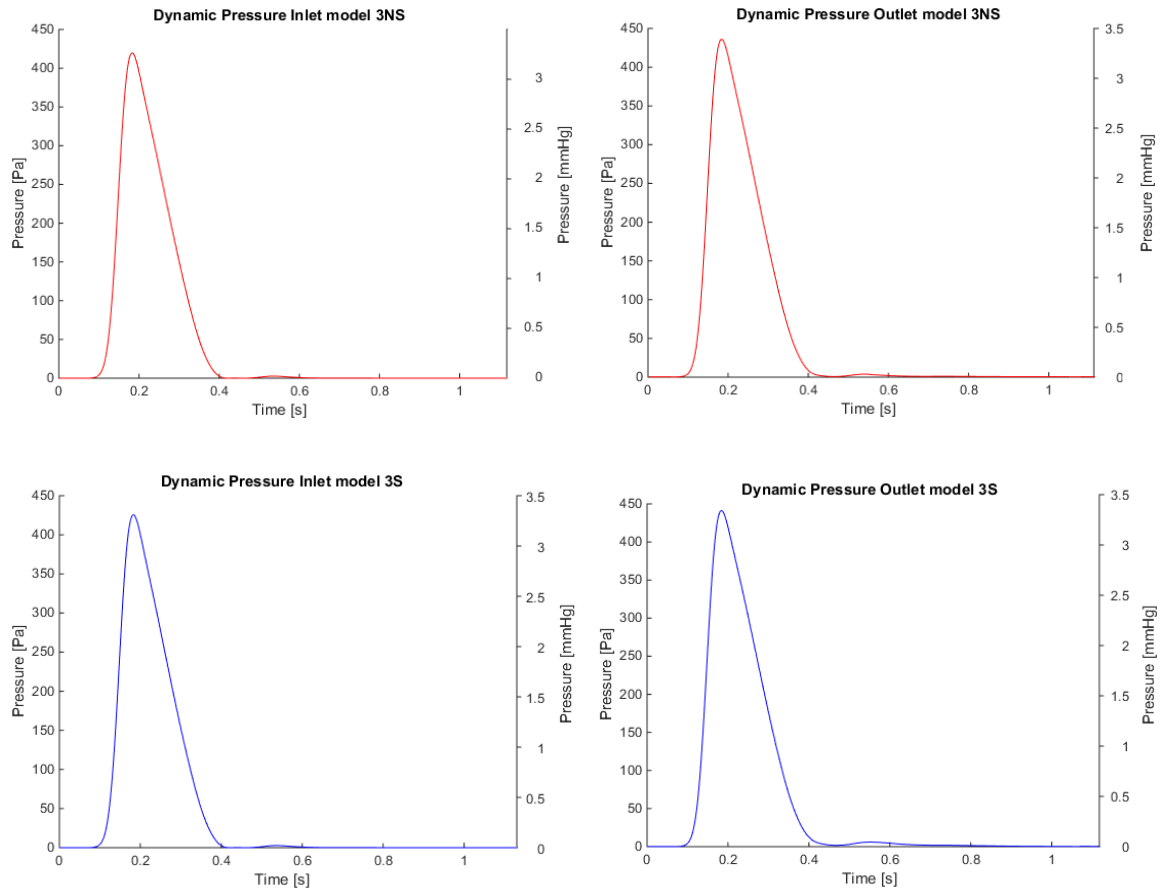


**Figure 3.28:** Dynamic pressure at inlet and outlet surface for model 3NS (red) and for 3S (blue)

# Chapter 4

## Discussion and Conclusions

The aim of this work was to investigate the efficacy of a single bare metal stent, in terms of induced hemodynamics and pressure distributions, in aortic districts with different geometries affected by aneurysmal disease.

Three arterial vessels with different curvatures were investigated: two models were idealized, and one was patient-specific. More in detail, the computational models of two vessels, with realistic aortic diameter, were constructed by using the software Solidworks®. The third model was reconstructed starting from medical images of a healthy human thoracic aorta. Basing on literature data, a fusiform-shape aneurysm was created at the bend of each vascular model. The investigating vascular device was modeled and inserted in the vascular districts by using Solidworks®. The unsteady-state fluid-dynamic simulations were conducted, with measured boundary conditions, by using the software Fluent®. The analysis was conducted by computing velocity distributions and, both WSS- and helicity-based descriptors (i.e., TAWSS, OSI, RRT, LNH,  $h$  indices).

The overall beneficial effect of the implanted stent can be appreciated by obtained pressure distributions (*Figure 3.20, 3.21 and 3.22*). In detail, for each investigated case, vessel stenting produces an increase of dynamic pressure at

the outlet section, with respect to the inlet one. This increase is due to the capability of the device to promote blood flow through the physiological lumen.

Looking at the obtained results, in terms of mean and peak systole velocity distributions, it can be noted that stent implantation markedly reduces blood flow into the aneurysm sac for all the investigated models. However, a relevant percentage of blood still flows through the aneurysm sac in models 2S and 3S, revealing the incapability of the investigated stent in efficaciously restore the physiological vascular lumen in highly curved vessels (*Figures 3.2 and 3.1*). The maps of LNH iso-surfaces confirm the inability of the investigated single layer stent in avoiding blood flowing into the aneurysm sac (*Figure 3.15*). *Figure 3.16* reveals the improvement of stent efficacy at higher velocities.

As concerns WSS-based descriptors, a significant decrease of TAWSS was observed at the aneurysmal wall for models 2S and 3S, compared to models 2 and 3, respectively. A decrease of TAWSS, even if weaker, was obtained for model 1, compared to its stented version (*Figure 3.5 and 3.6*). As TAWSS decreases, RRT rises after stent implantation, promoting blood particles deposition and preventing wall tearing (*Figure 3.13 and 3.14*).

Helicity-based descriptors showed the presence of counter-rotating structures, and considering LNH at peak systole, helical structures resulted mostly localized in the vascular lumen.

Many limitations affect this work. The investigated aneurysmal models are not patient-specific, but they were created basing on literature data. No supra-aortic vessels were included in the investigated models. Even if based on measured data, inflow boundary conditions were prescribed in terms of flat velocity profile.

In conclusion, the results of this work show that the efficacy of the investigated stent depends on the curvature of the vascular district. In detail, the analyzed vascular device results to work slightly better for straight vessels with respect to curved ones. In all the investigated districts, stent implantation leads to (1) a decrease of blood velocities in the aneurysm sac, preventing aneurysm rupture, and (2) an increase of dynamic pressure at the outlet sections of computational models with respect to the inlet ones. However, the here conducted analysis reveals the incapability of the investigated vascular device to efficaciously isolate the aneurysm sac, independently of vascular curvature. Results are encouraging, showing the capability of the investigated stent to

promote blood flowing through the physiological vascular lumen and suggesting some device design corrections. More in detail, a possible future development could consist in the optimization of stent weft in order to improve its efficacy in restoring physiological conditions in vascular districts affected by fusiform-shape aneurism formation. We suggest to investigate, in future, also, saccular-type aneurysms or the performance of multi-layer stents.

# Bibliography

- [1] Frank M Davis, Debra L Rateri, Alan Daugherty. Mechanisms of aortic aneurysm formation: translating preclinical studies into clinical therapies
  
- [2] George Koullias, MD,<sup>a</sup> Raj Modak MD,<sup>b</sup> Maryann Tranquilli, RN,<sup>a</sup> Dimitris P. Korkolis, MD,<sup>a</sup> Paul Barash, MD,<sup>a</sup> and John A. Elefteriades, MD<sup>a</sup>. Mechanical deterioration underlies malignant behavior of aneurysmal human ascending aorta
  
- [3] Wei Zeng Shan Huang and Chunshui He Chengdu. Endovascular Treatment of Thoracoabdominal Aorta Aneurysm by the Combination of a Stent Graft with Multiple Overlapping Bare Stents. *Elsevier Journal of Biomechanics*
  
- [4] Peng Zhang a, Anqiang Sun a,<sup>n</sup> Fan Zhan a, Jingyuan Luan b, Xiaoyan Deng. Hemodynamic study of overlapping bare-metal stents intervention to aortic aneurysm. *Elsevier Journal of Biomechanics 2014*
  
- [5] Yong-Xue Zhang, MD, Qing-Sheng Lu, MD, Jia-Xuan Feng, MD, Zhi-Qing Zhao, MD, Jun-Min Bao, MD, Rui Feng, MD, Xiang Feng, MD, and Zai-Ping Jing, MD. Endovascular management of pararenal aortic aneurysms with multiple overlapping uncovered stents *Annals of Vascular Surgery*
  
- [6] Peng Zhang, Xiao Liu, Anqiang Sun, Yubo Fan, Xiaoyan Deng Peng Zhang, Xiao Liu, Anqiang Sun, Yubo Fan, Xiaoyan Deng. Hemodynamic insight into overlapping baremetal stents strategy in the treatment of aortic aneurysm. *Elsevier Journal of Biomechanics 2015*
  
- [7] Eleni Metaxa, Konstantinos Tzirakis, Nikolaos Kontopodis, Christos V. Ioannou, Yannis Papaharilaou. Correlation of Intraluminal Thrombus Deposition. Biomechanics and Hemodynamics with Surface Growth and Rupture in Abdominal Aortic Aneurysm - Application in a Clinical Paradigm. *Annals of Vascular Surgery 2017*

- [8] Chi-Wei Ong, Pei Ho, and Hwa-Liang Leo. Effects of Microporous Stent Graft on the Descending Aortic Aneurysm: A Patient-Specific Computational Fluid Dynamics Study. *Artificial Organs*, Vol. 40, No. 11, 2016
- [9] Siang Lin Yeow and Hwa Liang Leo. Is Multiple Overlapping Uncovered Stents Technique Suitable for Aortic Aneurysm Repair? *Artificial Organs*, Vol. 42, No. 2, 2018
- [10] George S. Sfyroeras, MD, Ilias Dalainas, MD, Triantafyllos G. Giannakopoulos, MD, Konstantinos Antonopoulos, MD, John D. Kakisis, MD, and Christos D. Liapis, MD. Flow-diverting stent for the treatment of arterial aneurysm. *Journal of Vascular Surgery* 2012
- [11] Jean Marc Alsac, Frank R. Arko, Cristhopher K. Zarins TRATTAMENTO ENDOVASCOLARE DI ANEURISMI E DISSEZIONI DELL'AORTA TORACICA.
- [12] Mark F. Fillinger, MD, Steven P. Marra, PhD, M. L. Raghavan, PhD, and Francis E. Kennedy, PhD. Prediction of rupture risk in abdominal aortic aneurysm during observation: Wall stress versus diameter
- [13] Takafumi Akai, MD; Katsuyuki Hoshina, MD, PhD; Sota Yamamoto, PhD; Hiroaki Takeuchi, MEng; Youkou Nemoto, MD; Marie Ohshima, PhD; Kunihiro Shigematsu, MD, PhD; Tetsuro Miyata, MD, PhD; Haruo Yamauchi, MD, PhD; Minoru Ono, MD, PhD; Toshiaki Watanabe, MD, PhD. Biomechanical Analysis of an Aortic Aneurysm Model and Its Clinical Application to Thoracic Aortic Aneurysm for Defining "Saccular" Aneurysms. *Journal of the American Heart Association* 2017. *European Journal of Vascular/Endovascular Surgery*
- [14] John L. Anderson, FACS, FRACS Donald J. Adam, MD, FRCSE, Michael Berce, FRACS and David E. Hartley, FIR, FRANZCR (Hon). Repair of thoracoabdominal aortic aneurysms with fenestrated and branched endovascular stent grafts. *Journal of Vascular Surgery* 2005
- [15] Zhonghua Li, Clement Kleinstreuer. A comparison between different asymmetric abdominal aortic aneurysm morphologies employing

computational fluid–structure *European Journal of Mechanics B/Fluids* 26 (2007) 615–631

- [16] Zsolt Kulcsár & Luca Augsburger & Philippe Reymond & Vitor M. Pereira & Sven Hirsch & Ajit S. Mallik & John Millar & Stephan G. Wetzel & Isabel Wanke & Daniel A. Rüfenacht. Flow diversion treatment: intra-aneurismal blood flow velocity and WSS reduction are parameters to predict aneurysm thrombosis. *Acta Neurochir (2012) 154:1827*
- [17] Morris, F. Stefanov, N. Hynes, E.B. Diethrich, S. Sultan. An Experimental Evaluation of Device/Arterial Wall Compliance Mismatch for Four Stent-Graft Devices and a Multi-Layer Flow Modulator Device for the Treatment of Abdominal Aortic Aneurysms. *European Journal of Vascular/Endovascular Surgery (2016) 51, 44e55*
- [18] C. Mascoli, A. Freyrie, M. Gargiulo, E. Gallitto, R. Pini, G. Faggioli, C. Serra, C. De Molo, A. Stella a Selective Intra-procedural AAA sac Embolization During EVAR Reduces the Rate of Type II Endoleak. *European Journal of Vascular/Endovascular Surgery (2016) 51, 632e639*
- [19] Toshio Takayama, MD, PhD, Patrick J. Phelan, MD, and Jon S. Matsumura, MD, Madison, Wisc. Directional tip control technique for optimal stent graft alignment in angulated proximal aortic landing zones. *Midwestern Vascular Surgical Society*
- [20] Christos Lioupis, BSc, MSc, FEBVS, and Cherrie Z. Abraham, BSc, BA, MD, FRCSC. Results and Challenges for the Endovascular Repair of Aortic Arch Aneurysms. *Perspectives in Vascular Surgery and Endovascular Therapy 23(3) 202–213*
- [21] Yueh-Hsun Lu, Chia\_yuan Chen, Prahlad G. Menon, Kuan-Ting Liu, Hsing-Hung Lin. Hemodynamic Effects of Ebdoleak Formation in Abdominal Aneurysm Patients with Stent-Graft Implants. *Journal of Medical and Biological Engineering 34(6):554-558*
- [22] Zhonghua Li, Clement Kleinstreuer. Blood flow and structure interactions in a stented abdominal aortic aneurysm model. *Elsevier Journal of Biomechanics 2014*

- [23] Shuo Wang, Yongxue Zhang, Jiaxuan Feng, Yuan Huang, Aziz Tokgoz, Umar Sadat, Jonathan H. Gillard Qingsheng Lu, Zhongzhao Teng. Influence of overlapping pattern of multiple overlapping uncovered stents on the local mechanical environment: A patient-specific parameter study. *Elsevier Journal of Biomechanics* 60 (2017) 188–196
- [24] David A. Vorp. Biomechanics of abdominal aortic aneurysm. *Elsevier Journal of Biomechanics* 40 (2007) 1887–1902
- [25] Danny Bluesteina, Kris Dumonta, Matthieu De Beuleb, John Ricottac, Paul Impellizzeric, Benedict Verheghed and Pascal Verdonck. Intraluminal thrombus and risk of rupture in patient specific abdominal aortic aneurysm – FSI modelling. *Computer Methods in Biomechanics and Biomedical Engineering Vol. 12, No. 1, February 2009*, 73–81
- [26] April J. Boyd, MD, PhD, David C. S. Kuhn, PhD, Richard J. Lozowy, MSc and Gordon P. Kulbisky, MD. Low wall shear stress predominates at sites of abdominal aortic aneurysm rupture. *Journal of Vascular Surgery* 2015
- [27] Siobhan A. O'Leary, Eamon G. Kavanagh, Pierce A. Grace, Tim M. McGloughlin, Barry J. Doyle. The biaxial mechanical behavior of abdominal aortic aneurysm intraluminal thrombus: Classification of morphology and the determination of layer and region specific properties. *Journal of Biomechanics* 47(2014)1430–1437
- [28] E.S. Di Martino, G. Guadagni, A. Fumero, G. Ballerini, R. Spirito, P. Biglioli, A. Redaelli. Fluid–structure interaction within realistic three-dimensional models of the aneurysmatic aorta as a guidance to assess the risk of rupture of the aneurysm. *Medical Engineering & Physics* 23 (2001) 647–655
- [29] Corey J. Drewe, Louis P. Parker, Lachlan J. Kelsey, Paul E. Norman Janet T. Powell, Barry J. Doyle. Haemodynamics and stresses in abdominal aortic aneurysms: A fluid-structure interaction study into the effect of proximal neck and iliac bifurcation angle. *Elsevier Journal of Biomechanics* 60 (2017) 150–156
- [30] Michalis Xenos, Yared Alemu, Dan Zamfir, Shmuel Einav, John J. Ricotta, Nicos Labropoulos, Apostolos Tassiopoulos, Danny Bluestein.

The effect of angulation in abdominal aortic aneurysms: fluid-structure interaction simulations of idealized geometries. *Medical and Biological Engineering Computation* (2010) 48:1175–1190

- [31] Z. Li, C. Kleinstreuer. Analysis of biomechanical factors affecting stent-graft migration in an abdominal aortic aneurysm model. *Elsevier Journal of Biomechanics* 39 (2006) 2264–2273
- [32] Diego Gallo, David A. Steinman, Payam B. Bijari, and Umberto Morbiducci. Helical flow in carotid bifurcation as surrogate marker of exposure to disturbed shear. *Elsevier Journal of Biomechanics*, 45(14):2398–2404, 2012
- [33] Chi-Wei Ong, Pei Ho, and Hwa-Liang Leo. Effects of Microporous Stent Graft on the Descending Aortic Aneurysm: A Patient-Specific Computational Fluid Dynamics Study. *Artificial Organs* 2016, 40(11): E230–E240
- [34] Analysis of aortic wall stress and rupture risk in patients with abdominal aortic aneurysm with a gender perspective Emma Larsson, MD Fausto Labruto, MD, PhD, T. Christian Gasser, PhD, Jesper Swedenborg, MD, Prof and Rebecka Hultgren, MD, PhD, *JOURNAL OF VASCULAR SURGERY* August 2011
- [35] Relative importance of aneurysm diameter and body size for predicting abdominal aortic aneurysm rupture in men and women Ruby C. Lo, MD, Bing Lu, MD, PhD, Margriet T. M. Fokkema, MD, Mark Conrad, MD Virendra I. Patel, MD, Mark Fillinger, MD, Robina Matyal, MD, and Marc L. Schermerhorn, MD, on behalf of the Vascular Study Group of New England, *JOURNAL OF VASCULAR SURGERY* May 2014

# Ringraziamenti

Vorrei ringraziare, in primis, il Prof. Umberto Morbiducci e l'ing. Diego Gallo che mi hanno dato la possibilità di svolgere questa tesi, è stata lunga e dura ma ne è valsa la pena. Grazie anche perché mi hanno fatto scoprire ad amare questo splendido ambito del Cardiovascolare. Grazie anche e soprattutto a Giuseppe, l'ing. De Nisco, il tutor più buono, gentile e comprensivo che si possa desiderare, grazie per avermi sopportato e supportato in questi mesi, senza di te non ce l'avrei mai fatta. A questo proposito ringrazio anche le altre dottorande Paola e Karol che hanno contribuito in parte anche loro alla realizzazione di questa tesi.

Grazie alla mia famiglia, mio padre e mia sorella e tutti gli altri che mi hanno sempre incoraggiato e sostenuto avendo sempre fiducia in me, in particolare mia cugina Anna mia compagna di sventure.

Grazie ai miei coinquilini Mino, Rome, Fra e Scar mi avete regalato un anno meraviglioso, grazie per avermi sopportato ed aiutato sempre. Grazie ai vecchi coinquilini Jimbo, Darione, Gianlu, Richi, Nicols e il primo di tutti, Claudio che mi ha accolto a Torino. Jimbo, in particolare, in te ho scoperto uno dei miei più cari amici, buono, generoso e fedele, non so come farei senza di te, ormai sei come un fratello.

Grazie al Tarabbone, il mio amico torinese, onesto e fidato. Con te ho una libertà gigante e grazie a te sono riuscito a giudicare meglio la mia vita e ad affrontare questi anni al nord.

Grazie a Fra Villata, sei unica, fantastica, dolce e buona, la migliore amica che si possa desiderare. Grazie alla mia amica, marchigiana come me, Cate la nostra amicizia è proprio un dono grande, io per te ci sarò sempre e tu lo sai che potrai sempre contare su di me.

Grazie a Carli, Adri, Fra, e al vecchio appa di via Avigliana

Grazie a tutti gli amici del Poli e del Coro, mi mancherete

Grazie ai miei amici storici di infanzia: Gabri, Bea, Marco, Angi, Simo, Genius e Matti anche se ormai le nostre strade si stanno dividendo ci basta una serata insieme per capire che nulla è andato perduto.